Female Alms1-deficient mice develop echocardiographic features of adult but not infantile Alström Syndrome cardiomyopathy

McKay, Eleanor J; Luijten, Ineke ; Broadway-Stringer, Sophie; Thomson, Adrian; Weng, Xiong; Gehmlich, Katja; Gray, Gillian A.; Semple, Robert K

DOI:
10.1242/dmm.050561

Document Version
Peer reviewed version

Citation for published version (Harvard):
McKay, EJ, Luijten, I, Broadway-Stringer, S, Thomson, A, Weng, X, Gehmlich, K, Gray, GA & Semple, RK 2024, 'Female Alms1-deficient mice develop echocardiographic features of adult but not infantile Alström Syndrome cardiomyopathy', *Disease Models & Mechanisms*. https://doi.org/10.1242/dmm.050561

Female Alms1-deficient mice develop echocardiographic features of adult but not infantile Alström Syndrome cardiomyopathy

Eleanor J. McKay[1], Ineke Luijten[1], Sophie Broadway-Stringer[2], Adrian Thomson[1], Xiong Weng[1], Katya Gehmlich[2,3], Gillian A. Gray[1], Robert K. Semple[1,4,*]

[1]Centre for Cardiovascular Science, University of Edinburgh, Edinburgh, UK
[2]Institute of Cardiovascular Sciences, University of Birmingham, Birmingham B15 2TT, UK
[3]Division of Cardiovascular Medicine, Radcliffe Department of Medicine and British Heart Foundation Centre of Research Excellence Oxford, University of Oxford, Oxford, OX3 9DU, UK
[4]MRC Human Genetics Unit, Institute of Genetics and Cancer, University of Edinburgh, Edinburgh, UK

[*]**Correspondence to:**
Prof. Robert K. Semple, Centre for Cardiovascular Science, University of Edinburgh, Queen's Medical Research Institute, Little France Crescent, Edinburgh EH16 4TJ, UK. Tel: +44 131 242 6051/ Email: rsemple@ed.ac.uk

Abstract

Alström Syndrome (AS), a multisystem disorder caused by biallelic ALMS1 mutations, features major early morbidity and mortality due to cardiac complications. These are biphasic, including infantile dilated cardiomyopathy and distinct adult-onset cardiomyopathy, and are poorly understood. We assessed cardiac function of Alms1 knockout mice by echocardiography. Cardiac function was unaltered in global Alms1 knockout mice of both sexes at postnatal day 15 (P15) and 8 weeks. At 23 weeks, female, but not male knockout mice showed increased left atrial area and decreased isovolumic relaxation time, consistent with early restrictive cardiomyopathy, as well as reduced ejection fraction. No histological or transcriptional changes were seen in myocardium of 23-week-old female Alms1 global knockout mice. Female mice with Pdgfrα-Cre-driven Alms1 deletion in cardiac fibroblasts and a small proportion of cardiomyocytes did not recapitulate the phenotype of global knockout at 23 weeks. In conclusion, adult female, but not male, Alms1-deficient mice show echocardiographic evidence of cardiac dysfunction, consistent with the cardiomyopathy of AS. The explanation for sexual dimorphism remains unclear, but may involve metabolic or endocrine differences between sexes.

Disease Models & Mechanisms • DMM • Accepted manuscript

Keywords: ALMS1, Alström syndrome, Alstrom syndrome, heart, cardiomyopathy, ciliopathy, primary cilia

Introduction

Alström syndrome (AS) is an autosomal recessive disorder caused by biallelic loss-of-function mutations in the *ALMS1* gene. The product of the *ALMS1* gene is a large, 460 kDa protein primarily localised to the centrosome and basal body of primary cilia. In keeping with this, cardinal features of AS include infantile rod-cone retinal dystrophy, sensorineural deafness, obesity, and diabetes mellitus, which are common features of several so called primary "ciliopathies". AS also features prominent cardiac complications, which are a major cause of early morbidity and mortality in the syndrome (Marshall *et al.*, 2012).

Cardiac dysfunction occurs in approximately 60% of patients with AS at some point. The natural history of cardiac manifestations of AS is complicated, however, with a biphasic pattern across the lifecourse. Dilated cardiomyopathy and congestive heart failure occurs in 43% of infants with AS, usually reported in the first 12 months of life. In some cases this is fatal, but with treatment around three quarters of patients recover within 3 years (Marshall *et al.*, 2005). The mechanism of infantile cardiac dysfunction in AS is poorly understood. One clue was offered by identification of biallelic *ALMS1* mutations in four infants who died or underwent heart transplantation due to mitogenic cardiomyopathy, defined by persistent postnatal mitogenesis of cardiomyocytes (Louw *et al.*, 2014; Shenje *et al.*, 2014). Whether this was a sentinel presentation of AS is unknown, but similar histological appearances were reported in *Alms1*$^{GT/GT}$ mice harbouring a gene trap in intron 13, resulting in global knockout (KO) of *Alms1* (Shenje *et al.*, 2014). This remains the clearest potential explanation for the infantile heart failure of AS to date, but corroboratory studies are needed. How loss of ALMS1 expression might induce persistent mitogenesis is unknown.

Around 30% of adults with AS develop heart failure, in half of whom this is fatal or leads to transplantation (Marshall *et al.*, 2005; Paisey *et al.*, 2019). This appears independent of infantile cardiomyopathy (13% of patients develop both infantile and adult-onset cardiac dysfunction and 18% of patients only develop adult-onset dysfunction) (Marshall *et al.*, 2005; Corbetti *et al.*, 2013; Baig, Dowd, *et al.*, 2020). Adult-onset cardiomyopathy in AS features myocardial hypertrophy and dilation with progressive fibrosis and restrictive impairment of both ventricles (Marshall *et al.*, 2012). Accelerated atherosclerosis and coronary artery disease (CAD) are also reported (Jatti, Paisey and More, 2012; Paisey *et al.*, 2014, 2015; Baig, Dowd, *et al.*, 2020). Duration of diabetes in AS is predictive of aortic pulse wave velocity, and thus cardiovascular events (Paisey *et al.*, 2015), but no

association between CAD and cardiac fibrosis was found (Baig, Dowd, *et al.*, 2020). 63% of patients with AS develop chronic kidney disease (CKD) (Baig, Paisey, *et al.*, 2020), and 30% have hypertension (Marshall *et al.*, 2005; Waldman *et al.*, 2018), both further possible drivers of CAD.

Cardiac pathology in AS may thus be a composite result of cardiomyocyte-autonomous developmental defect in infancy, with accelerated atherosclerosis, and progressive fibrosis becoming prominent in young adulthood, driven in part by exogenous factors such as diabetes, insulin resistance, dyslipidaemia, hypertension and impaired renal function. Unpicking the relative contributions of these processes to the strikingly poor cardiovascular outcomes in AS is difficult or impossible in human studies where they are generally admixed. This issue is highly important as it will guide choice of experimental treatments for future trials in AS. For example, the high prevalence of cardiac fibrosis suggests potential value for anti-fibrotic therapies (Baig *et al.*, 2018), however whether fibrosis is a cause of cardiac dysfunction or an epiphenomenon arising from a chronic repair process in AS is unknown.

Understanding the cardiac phenotype of *Alms1* KO mice may be clinically relevant to patients with AS, and may also provide insights into common cardiac disease. In adults with AS, heart failure occurs alongside obesity, severe insulin resistance and shows preserved ejection fraction (Edwards *et al.*, 2015), similar to heart failure with preserved ejection fraction (HFpEF) for which metabolic syndrome is a major risk factor.

Several *Alms1* KO mouse lines have been described. These recapitulate many key features of AS, including vision and hearing loss, obesity and insulin resistant diabetes (Collin *et al.*, 2005; T Arsov *et al.*, 2006; Li *et al.*, 2007). Surprisingly, given its importance to patients with AS, no detailed evaluation of cardiac function in murine AS models has been offered to date. We thus set out to interrogate cardiac phenotypes across the lifecourse in a new *Alms1* global KO mouse model. To help distinguish heart autonomous and non-autonomous drivers of cardiac complications, we also studied mice with *Alms1* KO only in mesenchymal stem cells and their descendants using the constitutive *Pdgfrα*-Cre driver. This has been shown to drive recombination in cardiac fibroadipogenic precursor cells, such as cardiac fibroblasts, but only in 18% of cardiomyocytes (Lombardi *et al.*, 2016). *Pdgfrα*-Cre also drives recombination in preadipocytes and their descendants, in several brain regions (McKay *et al.*, 2023), but not in liver or muscle (Roesch *et al.*, 2008; Jeffery *et al.*, 2014; Krueger *et al.*, 2014). Conversely, publicly available single nuclear RNA sequencing data show low ALMS1/Alms1 expression in all cell types in the healthy adult human (Tucker *et al.*, 2020) and mouse (Speir *et al.*, 2021) heart.

Materials and Methods

Mouse strains and experimental protocols

Alms1$^{tm1c(EUCOMM)Hmgu}$ mice with loxP sites flanking exon 7 were generated by and purchased from GenOway, France. Excision of the floxed *Alms1* exon 7 yields a premature stop codon in exon 8. CAG-Cre mice (Sakai and Miyazaki, 1997) were a gift from Dr Matthew Brook and were used to generate a global *Alms1* KO. *Pdgfrα*-Cre mice (Roesch *et al.*, 2008) were purchased from The Jackson Laboratory (Strain #013148) and used to KO *Alms1* in mesenchymal stem cells. Although no reliable antibody against murine Alms1 was available to prove absence of Alms1 protein in the KO mice generated, recombination and loss of exon 7 of the *Alms1* transcript was confirmed both in genomic DNA (by Transnetyx, TN, USA) and in cDNA from heart (**Fig. S1A**), liver and adipose tissue (McKay *et al.*, 2023) by qPCR, as described in Supplementary Material. This is in line with previously published murine Alms1 KO models (**Table 1**).

All mice were purchased and maintained on a C57/BL6/N background, confirmed by single nucleotide polymorphism profiling (Transnetyx). Genotyping was performed by Transnetyx using real-time PCR in all cases except neonatal studies in which genotyping was performed in-house. In-house genotyping was performed by DNA gel electrophoresis following PCR amplification. One common forward primer (ATACCACCACACCTGGGAGG) and two reverse primers were used: reverse 1 (sequence contained in loxP flanked region; CACCATGTAAACACTAGAAATAGAACCCAGGTC) and reverse 2 (GCCAGGAGGAGCAAGACAAT). Presence of WT *Alms1* results in generation of a 366bp fragment by forward and reverse 1 primers. Excision of the loxP flanked sites results in the generation of a 306bp fragment by forward and reverse 2 primers.

Mice were group-housed in individually ventilated cages (IVCs) at the biological research facility at the University of Edinburgh. A 12-hour light/dark cycle (lights on at 0700 and off at 1900) and controlled temperature/humidity (19-21°C/50%) were maintained. Until 6 weeks old, mice had *ad libitum* access to standard chow (CRM, Special Diet Service), then replaced by 45% fat diet (D12451, Research Diets) to exacerbate systemic IR and any propensity to HFpEF, and to allow correlation with prior detailed metabolic studies undertaken on the same diet (McKay *et al.*, 2023). Mice were single housed from 13 weeks of age. All experimental protocols were approved by the University of Edinburgh Biological Science Services and performed in compliance with the UK Home Office Scientific Procedure (Animals) Act 1983. Echocardiography was performed by a single experienced operator at Edinburgh Preclinical Imaging.

Echocardiographic studies

For echocardiography mice were anaesthetised with 4% isoflurane in 100% oxygen for induction, with maintenance using 1-2% isoflurane. Animals were placed supine on a heated imaging table with paws attached to electrocardiogram (ECG) electrodes. Heart rate was maintained at 450-550 beats per minute (bpm), and never significantly differed between genotypes (**Figures S1I, S4Q,R, S5K**). Body temperature measured via rectal probe was maintained at 37±0.5°C using heated table and a heating lamp. Chest hair was removed using depilatory cream (Nair hair removal cream, Church & Dwight) and ultrasonography was performed using a VisualSonics Vevo 3100 high frequency ultrasound imaging system (FUJIFILM VisualSonics). An MX550D transducer was used except for obese mice at 23 weeks, where a lower frequency MX250 transducer with increased scan depth was required for Doppler measurements. For study of mice at P15.5, copper tape was used to extend the electrode pad to enable heart rate measurement, and an extra small rectal temperature probe was employed.

For left ventricle (LV) function assessment, electrocardiogram-gated Kilohertz visualisation (EKV (Moran *et al.*, 2013)) was applied on the parasternal long-axis (PSLA) view and for M-mode on the parasternal short axis (PSAX) view at LV midpoint with papillary muscles at 2 and 4 o'clock. Left atrium measurements were performed on EKV-modified right PSLA views. Doppler measurements of LV inflow and outflow were obtained in the apical 4 chamber view.

Electrocardiographic analysis

Analysis of echocardiographic data was performed using Visualsonics Vevo LAB 5.71 software (FUJIFILM VisualSonics). End systolic and end diastolic area, ejection fraction, fractional area change, left ventricle mass and average wall thickness were calculated from the PSLA EKV. End systolic and end diastolic area and ejection fraction were calculated using the automated artificial-intelligence software AutoLV (Grune *et al.*, 2019). Fractional area change, left ventricle mass and average wall thickness were calculated after manual tracing of the contours of PSLA epicardial and endocardial area and axis length at systole and diastole, as indicated by AutoLV. Fractional shortening was calculated from M-mode images using AutoLV. Modified right side PSLA EKV was used to manually measure left atrium area, choosing the time frame immediately after the mitral valve closure. Isovolumic relaxation time (IVRT), isovolumic relaxation time (IVCT) and ejection time (ET) were all calculated by manual analysis of Doppler; three consecutive annotations for each index were made. IVRT measures the time between aortic valve closing and the mitral valve opening. Myocardial

performance index (MPI) was calculated as the sum of IVRT and IVCT divided by ET. Finally, the 'Vevo Strain' function of the Vevo LAB software was used to analyse PSLA EKV, generating values for global longitudinal strain (GLS), reverse longitudinal strain rate (rLSR) and ventricular dyssynchrony. Ventricular dyssychrony was calculated as the standard deviation of strain across the 6 panels generated by 'Vevo Strain'.

For normalisation of size-dependent measurements (left ventricle mass, ventricle and atria areas), the nose-anus length and tibia length were measured using a digital calliper. Nose-anus length was measured when animals were anaesthetised for echocardiography at 23 weeks of age. Tibia length was measured following dissection at 24 weeks of age. As tibia length proved shorter in male and female global *Alms1* KO animals (**Fig. S3A**), nose-anus length, which did not differ by genotype (**Fig. S3B**), was used for normalisation. For normalisation of neonatal echocardiography, body mass was used, which did not differ between experimental groups.

Tissue studies

Mice were culled by cervical dislocation under isoflurane anaesthesia. Dissected hearts were rinsed in phosphate-buffered saline (PBS), and weighed after blotting of excess fluid. Whole neonatal hearts were fixed in 4% paraformaldehyde or snap-frozen in liquid nitrogen. The bottom 1/5th (apex) of adult hearts was fixed in 4% PFA, and the middle 2/5ths (ventricles) snap-frozen in liquid nitrogen. Adult tibia were also collected.

For histological analysis, fixed cardiac tissue was paraffin-embedded and 5µm sections cut. For picrosirius red (PSR) staining slides were dewaxed in xylene, rehydrated in decreasing concentrations of ethanol and washed in water before incubation in direct red picric acid solution for 2 hours, washing, dehydrating in ethanol, clearing in xylene, and mounting. Immunofluorescence staining of neonatal heart sections was performed using the Leica BOND III immunostainer robot at room temperature, with reagents detailed in **Table 2**. Sequential staining for histone H3, cardiac troponin (cTnT) and wheat germ agglutinin (WGA) was performed, with antibodies and conditions used detailed in **Table 3**. Washing with TBS-T buffer (composition) was performed between steps. For histone H3, antigen retrieval was by incubation in Bond Epitope Retrieval ER1 Solution (Leica Microsystems) for 20 minutes before peroxide blocking, blocking in diluted goat serum diluted 1:5 for 10 minutes. Anti-histone H3 antibody was incubated for 60 minutes before incubation with Goat Anti-Rabbit IgG HRP-conjugated secondary antibody for 30 minutes. Finally tyramide signal amplification was performed with addition of tyramide substrate FITC green opal 520. Next cTnT

staining was performed. Firstly antigen retrieval was performed by incubation in Bond Epitope Retrieval ER1 Solution for 10 minutes. Peroxide blocking was performed for 10 minutes followed by serum blocking for 10 minutes using blocking solution from the Mouse on Mouse Polymer IHC Kit (Abcam). Incubation of anti-cTnT was performed for 60 minutes before addition of secondary polymer from the Mouse on Mouse Polymer IHC Kit (Abcam) for 30 minutes. Finally, the tyramide substrate blue CY5 opal 650 was added. Next WGA staining was performed. Antigen retrieval was performed by incubation in Bond Epitope Retrieval ER1 Solution for 10 minutes. Peroxide blocking was then performed for 10 minutes before serum blocking in goat serum diluted 1:5 for 10 minutes. Rhodamine-conjugated WGA diluted 1:75 was then incubated for 60 minutes. Finally nuclear counter-staining was performed by incubation with DAPI, diluted 1:1000. All histological slides were imaged using a Zeiss Axioscan.Z1 with Zen2.6 software.

Gene expression analysis

RNA was extracted from snap-frozen heart tissue using the Qiagen RNeasy Fibrous Tissue Mini Kit after homogenisation in 2mL tubes containing 2.8mm ceramic beads stored on dry ice, using the Omni Bead Ruptor 24 Elite with the pre chilled Omni Cryo unit filled with dry ice. 10µL of RLT buffer was added per 1mg of heart tissue. 300µL homogenate was used for RNA extraction. After elution, RNA concentration was measured using the NanoDrop ONE before dilution to 100ng/µL in nuclease-free water. Reverse transcription was performed using the High Capacity cDNA Reverse Transcription Kit (Applied Biosystems) in the Eppendorf Mastercycler X50s, using 1000ng per reaction. cDNA solution was then diluted 1 in 4 with nuclease-free water. Control reactions without reverse transcriptase were performed alongside all experimental reactions.

Real-time quantitative PCR (RT-qPCR) was performed using TaqMan reagents on a LightCycler® 480 Instrument II (Roche) in duplex with minor groove binder (MGB) probes (Hein and Bodendorf, 2007). *Gapdh* was evaluated as a housekeeping control gene for normalisation using a 2'-chloro-7'phenyl-1,4-dichloro-6-carboxy-fluorescein (VIC)-coupled probe. Primer efficiency was calculated by dilution standard curve prior to experimental reactions. All reactions were run in triplicate, and RT- and non-template controls were run on the same plate. Crossing point (Cp) values were calculated using LightCycler 480 software using the Abs quant / 2nd derivative max function. Cp values for the gene of interest were normalised to duplexed *Gapdh* Cp values after adjusting for primer efficiency, as first described by Pfaffl (Pfaffl, 2001). Raw Cp values for the gene of interest and *Gapdh* were also visualised in all cases (e.g. **Fig. 3J, S2E**). Taqman primer and probe mixes used for qPCR were purchased from Life Technologies and are listed in **Table 4**.

Blinding and statistical analysis

Experimenter and analyser were blinded to genotype wherever possible, including for all *in vivo* studies, tissue processing, RNA extraction, imaging and analysis, and unblinding was automated by an Excel template to prevent accidental memorisation of genotypes. Statistical analysis was performed in GraphPad Prism 9.2.0. A normal distribution was assumed for all data, as the small numbers required by best practice in animal research preclude reliable testing for normality. Student's t-test was used for comparison of 2 groups and ANOVA for comparison of more than 2 groups. The Bonferroni correction was applied when multiple t-tests were performed. Šídák's multiple comparisons test was applied following ANOVA to data generated from the same animals at more than one time point, and Tukey's multiple comparison test following ANOVA to compare values between multiple groups. Linear regression was used to compare two experimental groups where the variable of interest depended on another variable that differed between groups (e.g. heart mass and body mass).

Results

We first set out to assess whether our novel global *Alms1* KO mouse model recapitulated the infantile cardiomyopathy of AS. One global *Alms1* KO mouse harbouring a gene trap in *Alms1* intron 13 has previously been reported to show persistent mitogenesis in the heart and increased heart to body mass ratio at postnatal day 15 (p15) (Shenje *et al.*, 2014), a timepoint roughly equivalent to the developmental age at human birth. This is in keeping with the mitogenic cardiomyopathy described in 4 infants with biallelic *ALMS1* loss-of-function mutations (Shenje *et al.*, 2014). We thus set out to seek corroboratory evidence for this in our newly generated global *Alms1* KO mouse, while extending the prior studies by characterising cardiac function by echocardiography. We elected to undertake functional studies at postnatal day 15 (p15) to replicate the prior study, and because this corresponds to an age of high prevalence of infantile cardiomyopathy in AS. In contrast to the previous study, however, no changes in heart to body mass ratio were observed in either male or female *Alms1* KO mice at p15 (**Fig. 1A,B**). Moreover the number of cardiomyocytes staining for the proliferative marker phosphorylated histone H3 (pH3), previously reported to be increased in myocardium of *Alms1* KO mice at p15 (Shenje *et al.*, 2014), did not differ between *Alms1* KO and WT littermates of either sex (**Fig. 1C,D**). Finally, no changes in a range of cardiac anatomical and functional measures obtained echocardiographically were seen. These included left ventricular mass, wall thickness and chamber dimensions (**Fig. 1E-G, Fig. S1B,C**), measures of systolic and

diastolic function, longitudinal strain and ventricular dyssynchrony (Bilchick et al., 2006) (**Fig. 1H-J, Fig. S1D-H**).

Consistent with the normal echocardiographic and histological appearances of hearts at P15, transcriptional analysis of myocardium for a panel of markers of heart failure, namely actin alpha 1 (*Acta1)*; myosin heavy chain beta (*Myh7)*; and natriuretic peptides A and B, (*Nppa* and *Nppb)* (**Fig. S2A-D**), normalised to *Gapdh* (e.g. **Fig. S2E**), showed no clear indications of cardiac dysfunction. An isolated increase in *Myh7* expression between female WT and *Alms1* KO mice is not consistent with expression of the other genes and is of uncertain importance. Collectively these findings provide no evidence of mitogenic or other forms of infantile cardiomyopathy in the new global *Alms1* KO mouse strain.

We next sought to assess cardiac function in global *Alms1* KO mice in adulthood, at both 8 weeks and 23 weeks of age, with tissue collection at 24 weeks of age. These ages correspond roughly to the second and fourth decades of human life, periods in which AS cardiomyopathy is commonly seen. Both male (**Fig. 2A**) and female (**Fig. 2C**) absolute heart masses were increased at 24 weeks of age, however linear regression showed this increase to be proportionate to body mass, which is higher in AS and *Alms1* KO mice. No changes in echocardiographic anatomical or functional indices were observed in either male or female mice at 8 weeks of age (**Fig. 2B,D-L, Fig. S3C-R**). At 23 weeks of age, however, the left atrial area of female mice, a well-established indirect indicator of diastolic cardiac dysfunction, was increased compared to WT littermate controls (**Fig. 2D**). Typically, diastolic dysfunction is also characterised by increased isovolumic relaxation time (IVRT) and/or decreased reverse longitudinal strain rate (Schnelle *et al.*, 2018). However in the more unusual case of restrictive diastolic dysfunction, decreased IVRT and/or increased reverse longitudinal strain rate have been shown to be good additional indicators in the diseased mouse heart when in conjunction with increased left atrial size (Schnelle *et al.*, 2018). In agreement with clinical reports of restrictive diastolic dysfunction in patients with AS (Paisey *et al.*, 1993), we found that IVRT was indeed decreased in female mice at 23 weeks of age (**Fig. 2L**), while reverse longitudinal strain rate showed no significant difference (**Fig. S4O**).

E/A and E/e' ratios, of value in humans and larger rodents as further indices of diastolic function, could not be evaluated as E and A waves are fused at physiological murine heart rates of 450-600bpm, in line with prior findings in multiple models (Schnelle *et al.*, 2018). In male mice at 23 weeks of age no significant differences in echocardiographic indices was seen, though a trend to increased left atrial area and reduced IVRT was observed (**Fig. 2B,J**).

Female global *Alms1* KO mice at 23 weeks also showed several other cardiac functional changes suggestive of systolic dysfunction compared to WT littermate controls, including reduced ejection fraction, and fractional ventricular area change (**Fig. 2G,H**). Fractional shortening showed a trend towards reduction (**Fig. 2K**). Again, all these indices were unchanged in male mice (**Fig. 2B,E,F,I,J**). Left ventricle mass, wall thickness, cross-sectional areas, performance index, longitudinal strain and dyssynchrony were unchanged in both sexes at 23 weeks of age (**Fig. S3C-R**).

Transcriptional analysis of hearts at 24 weeks of age was next undertaken to evaluate markers of cardiomyopathy, as before, with addition of two genes associated with fibrosis, alpha-1 type I collagen (*Col1a1)* and lysyl oxidase (*Lox)*, and three genes involved in cell cycle regulation and cellular senescence, cyclin dependent kinase inhibitor 1A (*Cdkn1a*), cyclin dependent kinase inhibitor 2A (*Cdkn2a*) and lamin B1 (*Lmnb1)*. No changes in expression of any of these genes were seen between female global *Alms1* KO mice and WT littermates (**Fig. 3A-I**) when normalised to Gapdh (e.g. **Fig. 3J**). Global *Alms1* KO male mice did show decreased transcript levels of *Lmnb1* (**Fig. 3I**). However although reduced *Lmnb1* expression is one marker of cellular senescence, *Cdkn1a* and *Cdkn2a* transcripts, which are typically elevated in senescence, were decreased or showed a trend in this direction (p=0.15 for *Cdkn1a*), arguing against established senescence (**Fig. 3G,H**). There were no changes in genes typically associated with heart failure or fibrosis in the male *Alms1* KO mice (**Fig. 3A-F**). In keeping with unchanged transcript levels for fibrosis-associated genes, no increase in picrosirius red staining for fibrosis was seen (**Fig. 3K**).

Finally, in order to assess the contribution of different cell populations to the cardiac dysfunction seen in female mice at 23 weeks of age, the cardiac phenotype of mice in which *Alms1* KO was driven by the *Pdgfrα* promoter, a marker of mesenchymal stem cells, was evaluated. As would be expected from loss of *Alms1* in cardiac fibroblasts and ~18% cardiomyocytes, *Alms1* myocardial transcript levels were significantly decreased but not completely lost in hearts of female MSC-specific *Alms1* KO mice (**Fig. S4A**). Similar to female global *Alms1* KO mice, heart mass was proportionate to body mass in female MSC-specific *Alms1* KO animals (**Fig. 4A**), but in contrast to female global *Alms1* KO mice, female MSC-specific *Alms1* KO mice did not show differences in left atrial area, ejection fraction, fractional area change nor fractional shortening on echocardiography (**Fig. 4B-E**). A decrease in isovolumic relaxation time did remain in MSC-specific *Alms1* KO mice (**Fig. 4F**), but all other echocardiographic indices were unchanged (**Fig. S4C-J**) except myocardial performance index, which was decreased (**Fig. S4G**).

Discussion

This study generated two *in vivo* models of AS, namely a new global KO and an MSC-specific *Alms1* KO, both derived from the same *Alms1* floxed parental line. Both were extensively characterised with respect to cardiac structure and function at multiple time points. Despite the prominence of cardiomyopathy in AS, and the high importance assigned to improving understanding of this by patients and families, such analysis has not been reported for any prior *Alms1* KO model. We find that, at 23 weeks of age, global *Alms1* KO female mice do show evidence of systolic dysfunction (reduced ejection fraction, fractional area change and fractional shortening), although neither myocardial performance index nor global longitudinal strain were significantly changed. An unusual form of diastolic dysfunction was suggested by the combination of increased left atrial area and decreased isovolumic relaxation time, which has previously been reported in models with restrictive diastolic dysfunction (Schnelle *et al.*, 2018). This is in accord with clinical reports of cardiac dysfunction in AS (Paisey *et al.*, 1993). However reverse longitudinal strain rate, another indicator of diastolic dysfunction, showed no significant difference.

Despite the echocardiographic abnormalities seen in female global *Alms1* KO mice at 23 weeks of age, no corresponding transcriptional or histological changes were detected in myocardial tissue, including no evidence of increased fibrosis or senescence. Nevertheless our findings collectively do indicate mild combined systolic and diastolic dysfunction, reminiscent of the restrictive cardiomyopathy of AS (Paisey *et al.*, 1993), at least in adult female *Alms1* KO mice. As age is an important cofactor in development of AS cardiomyopathy, it is plausible that more pronounced cardiac dysfunction may become manifest at more advanced ages.

In contrast to findings in older female KO mice, no phenotype was observed in male *Alms1* KO mice at the same age. This is notable, as males have been found to be more severely affected than females for several mouse models of genetic cardiomyopathy (Du, 2004; Shinlapawittayatorn *et al.*, 2022). No sexual dimorphism in cardiac pathology in human AS has been reported (Baig, Dowd, *et al.*, 2020). Diastolic dysfunction has been associated with non-cardiac drivers such as hypertension, diabetes, and obesity (Noll, Lal and Merryman, 2020), and we have reported that the line of global *Alms1* KO mice studied here, like other global KO models described previously, is obese and insulin resistant (McKay *et al.*, 2023). The difference in these metabolic traits is much more pronounced between female wild-type and KO mice than between male counterparts, and male KO mice are severely insulin resistant but not hyperglycaemic (McKay *et al.*, 2023). This implicated metabolic differences as one possible cause of the sexual dimorphism we describe in the *Alms1* KO cardiac phenotype. In keeping with this, Heart Failure with preserved Ejection Fraction (HFpEF), which is

associated with diabetes, is more prominent in females than males (Sotomi *et al.*, 2021), while diabetes increases the risk of heart failure twice as much in females as in males (Kannel, Hjortland and Castelli, 1974). Although no correlation has been found cross sectionally between metabolic dysregulation and cardiac dysfunction in human AS, numbers studied have been very small (Brofferio *et al.*, 2017).

To narrow the search for the cellular origin of the cardiac phenotype of older female global *Alms1* KO mice, we also studied female mice with *Alms1* KO driven by *Pdgfra*-cre. This has been shown to delete *Alms1* in a raft of mesenchymal stem cells, including cardiac fibroadipogenic precursors, while largely sparing cardiomyocytes (Lombardi *et al.*, 2016). In this study the indices of systolic and diastolic dysfunction seen in female global *Alms1* KO mice were not recapitulated by female MSC-specific *Alms1* KO mice. Significantly, these conditional KO mice do also have insulin resistance and diabetes (McKay *et al.*, 2023). This is counter to the suggestion that the sexually dimorphic cardiomyopathy in female *Alms1* KO mice is purely metabolically mediated, instead indicating that cardiomyocyte-autonomous *Alms1* deficiency plays an important, and perhaps dominant role. Cardiomyocyte-specific *Alms1* KO could be used to confirm this in future.

One limitation of this study is that confirmation of complete loss of Alms1 protein was not possible, as no antibody against murine Alms1 is available. We did, however, confirm frameshifting deletion of exon 7 at both genomic DNA and cDNA level. Lack of protein-level knockout confirmation is true also of prior knockout models, and moreover non cardiac features of Alström syndrome are well modelled and consistent across all models. On this basis we think the possibility that our findings are confounded by residual Alms1 expression is negligible. A further limitation of this study is that blood pressure was not measured. *Alms1* KO rats are reported to be hypertensive, attributed to altered tubular trafficking of the Na-K-Cl channel, and hypertension is observed in around 30% of patients with AS (Marshall *et al.*, 2005; Edwards *et al.*, 2015; Brofferio *et al.*, 2017). It is thus highly plausible that our new KO line, too, features hypertension, and future assessment of this in this model is warranted.

This study did not find evidence of cardiomyopathy in *Alms1* KO mice at P15, at odds both with the previous demonstration in *Alms1*$^{GT/GT}$ mice of increased heart/body mass ratio and persistent cardiomyocyte mitosis, and with mitogenic cardiomyopathy in four infants with biallelic *ALMS1* mutations (Shenje *et al.*, 2014). Given the good concordance of several important phenotypic features of AS among different *Alms1* KO mice models, it was surprising that this early cardiac phenotype could not be replicated. The discrepancy between studies of AS-related infantile cardiomyopathy may relate to genetic background, as the prior study used mice with a mixed

129/C57BL6/J background. Genetic background has been shown to influence other murine cardiac phenotypes (Shah *et al.*, 2010; Riehle and Bauersachs, 2019; Hart *et al.*, 2022), while the incomplete penetrance (43%) of infantile cardiomyopathy in AS also argues that environmental or background genetic factors may play a role in human expression of AS cardiomyopathy. Cardiomyocyte binucleation is typically complete by p10 in WT mice (Shenje *et al.*, 2014), and it remains possible that a difference in trajectory of cardiomyocyte maturation would have been discerned if an earlier time point had been studied. Indeed, infantile cardiomyopathy in patients with AS commonly spontaneously recovers, in keeping with a self-limiting alteration of maturation kinetics. Future studies of *Alms1* KO mice incorporating multiple early postnatal time-points may thus be informative.

In toto, although we detect early cardiac abnormalities in 23 week old female global *Alms1* KO mice, this study demonstrates that mice do not faithfully replicate the severe biphasic cardiomyopathy common in human AS. This may reflect a fundamental inter-species difference in the consequences of *Alms1* loss, undermining the future utility of mouse models for its study. Alternatively, it may be revealing about the relative contributions of different pathogenic mechanisms to heart failure in human AS. Two pertinent differences between C57BL6/N mice and humans are that that the mice are neither extremely fibrosis- (Walkin *et al.*, 2013) nor atherosclerosis-prone. The absence of a severe cardiac phenotype in mice could thus be interpreted as strengthening the case that accelerated atherosclerosis, and/or pathological abnormalities in remodelling in the face of ischaemia, and/or excess fibrosis are the dominant drivers of adult heart failure in AS.

Several other murine models of cardiomyopathy model human disease poorly (e.g. (Vignier *et al.*, 2009; Ehsan *et al.*, 2018; Jiang *et al.*, 2021)). Several measures are worthy of consideration in future to increase the value of the *Alms1* KO mouse as a cardiac disease model. These include increasing the age of the mice studied, as age is an important factor in development of diastolic dysfunction (Riehle and Bauersachs, 2019; Noll, Lal and Merryman, 2020), or using pharmacological stressors such as angiotensin II or adrenergic agonists (Pilz *et al.*, 2022) to 'unmask' cardiac dysfunction. More specific options to gain insights into AS heart failure pathogenesis include examining *Alms1* KO on either an atherosclerosis-prone (e.g. *Apoe*$^{-/-}$ or *Pcsk9*$^{-/-}$) or fibrosis-prone (S129S6) genetic background. Our findings, however, underline the value of alternative experimental models of the cardiac complications of AS, including for example the induced pluripotent stem cell-derived cardiomyocytes. Continuing to optimise models of cardiac complications of AS will be crucial not only for unpicking and more effectively targeting devastating complications of an ultra-rare disease,

but may also yield prismatic insights into the role of complex multi-morbidities (e.g. diabetes, obesity, kidney and liver impairment) in more common conditions such as HFpEF.

Funding

EM is supported by a British Heart Foundation (BHF) PhD studentship [FS/18/57/34178], RKS by the Wellcome Trust [210752] and the BHF Centre for Research Excellence Award III [RE/18/5/34216], and IL by the Swedish Research Council (2019-06422). KG is supported by the Medical Research Council [MR/V009540/1]. The Institute of Cardiovascular Sciences, University of Birmingham, has received an Accelerator Award by the British Heart Foundation [AA/18/2/34218]. Edinburgh Preclinical Imaging is supported by the Wellcome Trust [212923/Z/18/Z].

Author Contributions

EJM: conceptualisation, methodology, formal analysis, investigation, writing - original draft, writing - review & editing, visualization; **IL**: supervision, writing - review & editing; **SB-S**: writing - review & editing; **AT:** methodology, formal analysis, investigation; **XW**: investigation; **KG:** methodology, writing - original draft, writing - review & editing; **GG:** writing - original draft, writing - review & editing, supervision; **RKS:** conceptualisation, methodology, resources, writing - original draft, writing - review & editing, supervision, funding acquisition.

Conflict of interest

RKS has received consulting fees from Novartis, Astra Zeneca, and Alnylam, research contribution in kind from Pfizer, and speaking fees from Novo Nordisk, Eli Lilly, and Amryt

References

Arsov, Todor, Larter, C.Z., *et al.* (2006) 'Adaptive failure to high-fat diet characterizes steatohepatitis in Alms1 mutant mice', *Biochemical and Biophysical Research Communications*, 342(4), pp. 1152–1159. Available at: https://doi.org/10.1016/j.bbrc.2006.02.032.

Arsov, Todor, Silva, D.G., *et al.* (2006) 'Fat aussie - A new Alström syndrome mouse showing a critical role for ALMS1 in obesity, diabetes, and spermatogenesis', *Molecular Endocrinology*, 20(7), pp. 1610–1622. Available at: https://doi.org/10.1210/me.2005-0494.

Arsov, T *et al.* (2006) 'Fat aussie--a new Alstrom syndrome mouse showing a critical role for ALMS1 in obesity, diabetes, and spermatogenesis', *Mol Endocrinol*. 2006/03/04, 20(7), pp. 1610–1622. Available at: https://doi.org/10.1210/me.2005-0494.

Baig, S. *et al.* (2018) 'Treatment with PBI-4050 in patients with Alström syndrome: study protocol for a phase 2, single-Centre, single-arm, open-label trial.', *BMC endocrine disorders*, 18(1), p. 88. Available at: https://doi.org/10.1186/s12902-018-0315-6.

Baig, S., Paisey, R., *et al.* (2020) 'Defining renal phenotype in Alström syndrome', *Nephrology Dialysis Transplantation*, 35(6), pp. 994–1001. Available at: https://doi.org/10.1093/ndt/gfy293.

Baig, S., Dowd, R., *et al.* (2020) 'Prospective cardiovascular magnetic resonance imaging in adults with Alström syndrome: silent progression of diffuse interstitial fibrosis', *Orphanet Journal of Rare Diseases*, 15(1), p. 139. Available at: https://doi.org/10.1186/s13023-020-01426-4.

Brofferio, A. *et al.* (2017) 'Characteristics of cardiomyopathy in Alström syndrome: Prospective single-center data on 38 patients', *Molecular Genetics and Metabolism*, 121(4), pp. 336–343. Available at: https://doi.org/10.1016/j.ymgme.2017.05.017.

Brun, A. *et al.* (2019) 'In vivo phenotypic and molecular characterization of retinal degeneration in mouse models of three ciliopathies', *Experimental Eye Research*, 186. Available at: https://doi.org/10.1016/j.exer.2019.107721.

Collin, G.B. *et al.* (2005) 'Alms1-disrupted mice recapitulate human Alström syndrome', *Human Molecular Genetics*, 14(16), pp. 2323–2333. Available at: https://doi.org/10.1093/hmg/ddi235.

Corbetti, F. *et al.* (2013) 'Alström Syndrome: Cardiac Magnetic Resonance findings', *International Journal of Cardiology*, 167(4), pp. 1257–1263. Available at: https://doi.org/10.1016/j.ijcard.2012.03.160.

Du, X.J. (2004) 'Gender modulates cardiac phenotype development in genetically modified mice', *Cardiovascular Research*, pp. 510–519. Available at: https://doi.org/10.1016/j.cardiores.2004.03.027.

Edwards, N.C. *et al.* (2015) 'Diffuse left ventricular interstitial fibrosis is associated with sub-clinical myocardial dysfunction in Alström Syndrome: An observational study', *Orphanet Journal of Rare Diseases*, 10(1), p. 83. Available at: https://doi.org/10.1186/s13023-015-0292-z.

Ehsan, M. *et al.* (2018) 'Mutant Muscle LIM Protein C58G causes cardiomyopathy through protein depletion.', *Journal of molecular and cellular cardiology*, 121, pp. 287–296. Available at: https://doi.org/10.1016/j.yjmcc.2018.07.248.

Farrell, G.C. *et al.* (2014) 'Strain dependence of diet-induced NASH and liver fibrosis in obese mice is linked to diabetes and inflammatory phenotype', *Liver International*, 34(7), pp. 1084–1093. Available at: https://doi.org/10.1111/liv.12335.

Favaretto, F. *et al.* (2014) 'GLUT4 defects in adipose tissue are early signs of metabolic alterations in alms1GT/GT, a mouse model for obesity and insulin resistance', *PLoS ONE*, 9(10), p. e109540. Available at: https://doi.org/10.1371/journal.pone.0109540.

Geberhiwot, T. *et al.* (2021) 'Relative Adipose Tissue Failure in Alström Syndrome Drives Obesity-Induced Insulin Resistance', *Diabetes*, 70(2), pp. 364–376. Available at: https://doi.org/10.2337/db20-0647.

Grune, J. *et al.* (2019) 'Accurate assessment of LV function using the first automated 2D-border detection algorithm for small animals - evaluation and application to models of LV dysfunction', *Cardiovascular Ultrasound*, 17(1), p. 7. Available at: https://doi.org/10.1186/s12947-019-0156-0.

Hart, C.C. *et al.* (2022) 'Evaluation of the DBA/2J mouse as a potential background strain for genetic models of cardiomyopathy', *Journal of Molecular and Cellular Cardiology Plus*, 1, p. 100012. Available at: https://doi.org/10.1016/J.JMCCPL.2022.100012.

Hein, A.E. and Bodendorf, U. (2007) 'Real-time PCR: duplexing without optimization.', *Analytical biochemistry*, 360(1), pp. 41–46. Available at: https://doi.org/10.1016/j.ab.2006.10.016.

Jagger, D. *et al.* (2011) 'Alström Syndrome protein ALMS1 localizes to basal bodies of cochlear hair cells and regulates cilium-dependent planar cell polarity', *Hum Mol Genet*. 11/11, 20(3), pp. 466–481. Available at: https://doi.org/10.1093/hmg/ddq493.

Jatti, K., Paisey, R. and More, R. (2012) 'Coronary artery disease in Alström syndrome', *European Journal of Human Genetics*, 20(1), pp. 117–118. Available at: https://doi.org/10.1038/ejhg.2011.168.

Jeffery, E. *et al.* (2014) 'Characterization of Cre recombinase models for the study of adipose tissue', *Adipocyte*, 3(3), pp. 206–211. Available at: https://doi.org/10.4161/adip.29674.

Jiang, H. *et al.* (2021) 'Functional analysis of a gene-edited mouse model to gain insights into the disease mechanisms of a titin missense variant', *Basic Research in Cardiology*, 116(1), pp. 1–18. Available at: https://doi.org/10.1007/s00395-021-00853-z.

Kannel, W.B., Hjortland, M. and Castelli, W.P. (1974) 'Role of diabetes in congestive heart failure: The Framingham study', *The American Journal of Cardiology*, 34(1), pp. 29–34. Available at: https://doi.org/10.1016/0002-9149(74)90089-7.

Krueger, K.C. *et al.* (2014) 'Characterization of cre recombinase activity for in vivo targeting of adipocyte precursor cells', *Stem Cell Reports*, 3(6), pp. 1147–1158. Available at: https://doi.org/10.1016/j.stemcr.2014.10.009.

Larter, C.Z. *et al.* (2009) 'Roles of adipose restriction and metabolic factors in progression of steatosis to steatohepatitis in obese, diabetic mice', *J Gastroenterol Hepatol*. 2009/10/01, 24(10), pp. 1658–1668. Available at: https://doi.org/10.1111/j.1440-1746.2009.05996.x.

Larter, C.Z. *et al.* (2012) 'Peroxisome proliferator-activated receptor-α agonist, Wy 14643, improves metabolic indices, steatosis and ballooning in diabetic mice with non-alcoholic steatohepatitis', *Journal of Gastroenterology and Hepatology (Australia)*, 27(2), pp. 341–350. Available at: https://doi.org/10.1111/j.1440-1746.2011.06939.x.

Li, G. *et al.* (2007) 'A role for Alström syndrome protein, Alms1, in kidney ciliogenesis and cellular quiescence', *PLoS Genetics*. 2007/01/09, 3(1), p. e8. Available at: https://doi.org/10.1371/journal.pgen.0030008.

Lombardi, R. *et al.* (2016) 'Cardiac fibro-adipocyte progenitors express desmosome proteins and preferentially differentiate to adipocytes upon deletion of the desmoplakin gene', *Circulation Research*, 119(1), pp. 41–54. Available at: https://doi.org/10.1161/CIRCRESAHA.115.308136.

Louw, J.J. *et al.* (2014) 'Homozygous loss-of-function mutation in ALMS1 causes the lethal disorder mitogenic cardiomyopathy in two siblings', *European Journal of Medical Genetics*, 57(9), pp. 532–535. Available at: https://doi.org/https://doi.org/10.1016/j.ejmg.2014.06.004.

Marshall, J.D. *et al.* (2005) 'New Alström Syndrome Phenotypes Based on the Evaluation of 182 Cases', *Archives of Internal Medicine*, 165(6), pp. 675–683. Available at: https://doi.org/10.1001/archinte.165.6.675.

Marshall, J.D. *et al.* (2012) 'Alstrom Syndrome: Genetics and Clinical Overview', *Current Genomics*, 12(3), pp. 225–235. Available at: https://doi.org/10.2174/138920211795677912.

McKay, E.J. *et al.* (2023) 'Mesenchymal-specific Alms1 knockout in mice recapitulates key metabolic features of Alström Syndrome', *bioRxiv*, p. 2023.10.12.562074. Available at: https://doi.org/10.1101/2023.10.12.562074.

Moran, C.M. *et al.* (2013) 'High-resolution echocardiography in the assessment of cardiac physiology and disease in preclinical models', *Experimental Physiology*, 98(3), pp. 629–644. Available at: https://doi.org/10.1113/expphysiol.2012.068577.

Noll, N.A., Lal, H. and Merryman, W.D. (2020) 'Mouse Models of Heart Failure with Preserved or Reduced Ejection Fraction', *American Journal of Pathology*, pp. 1596–1608. Available at: https://doi.org/10.1016/j.ajpath.2020.04.006.

Paisey, R.B. *et al.* (1993) *Alström Syndrome*, *GeneReviews®*. Edited by M.P. Adam et al. Seattle (WA). Available at: http://www.ncbi.nlm.nih.gov/pubmed/22303800.

Paisey, R.B. *et al.* (2014) 'Modification of severe insulin resistant diabetes in response to lifestyle changes in Alström syndrome', *European Journal of Medical Genetics*, 57(2–3), pp. 71–75. Available at: https://doi.org/10.1016/j.ejmg.2013.12.008.

Paisey, R.B. *et al.* (2015) 'Duration of Diabetes Predicts Aortic Pulse Wave Velocity and Vascular Events in Alstrom Syndrome', *J Clin Endocrinol Metab*. 2015/06/13, 100(8), pp. E1116-24. Available at: https://doi.org/10.1210/jc.2015-1577.

Paisey, R.B. *et al.* (2019) 'Alström Syndrome', in *GeneReviews® [Internet]*. University of Washington, Seattle.

Pfaffl, M.W. (2001) 'A new mathematical model for relative quantification in real-time RT-PCR.', *Nucleic acids research*, 29(9), p. e45. Available at: https://doi.org/10.1093/nar/29.9.e45.

Pilz, P.M. *et al.* (2022) 'Large and Small Animal Models of Heart Failure With Reduced Ejection Fraction', *Circulation Research*, 130(12), pp. 1888–1905. Available at: https://doi.org/10.1161/CIRCRESAHA.122.320246.

Poekes, L. *et al.* (2017) 'Defective adaptive thermogenesis contributes to metabolic syndrome and liver steatosis in obese mice', *Clinical Science*, 131(4), pp. 285–296. Available at: https://doi.org/10.1042/CS20160469.

Riehle, C. and Bauersachs, J. (2019) 'Small animal models of heart failure', *Cardiovascular Research*. Oxford Academic, pp. 1838–1849. Available at: https://doi.org/10.1093/cvr/cvz161.

Roesch, K. *et al.* (2008) 'The transcriptome of retinal Müller glial cells', *Journal of Comparative Neurology*, 509(2), pp. 225–238. Available at: https://doi.org/10.1002/cne.21730.

Sakai, K. and Miyazaki, J.I. (1997) 'A transgenic mouse line that retains Cre recombinase activity in mature oocytes irrespective of the cre transgene transmission', *Biochemical and Biophysical Research Communications* [Preprint]. Available at: https://doi.org/10.1006/bbrc.1997.7111.

Schnelle, M. *et al.* (2018) 'Echocardiographic evaluation of diastolic function in mouse models of heart disease', *Journal of Molecular and Cellular Cardiology*, 114, pp. 20–28. Available at: https://doi.org/10.1016/j.yjmcc.2017.10.006.

Shah, A.P. *et al.* (2010) 'Genetic background affects function and intracellular calcium regulation of mouse hearts', *Cardiovascular Research*, 87(4), pp. 683–693. Available at: https://doi.org/10.1093/CVR/CVQ111.

Shenje, L.T. *et al.* (2014) 'Mutations in Alström protein impair terminal differentiation of cardiomyocytes', *Nature Communications*, 5(1), p. 3416. Available at: https://doi.org/10.1038/ncomms4416.

Shinlapawittayatorn, K. *et al.* (2022) 'Sexual dimorphism in cardiometabolic and cardiac mitochondrial function in obese rats following sex hormone deprivation', *Nutrition and Diabetes*, 12(1). Available at: https://doi.org/10.1038/s41387-022-00189-0.

Sotomi, Y. *et al.* (2021) 'Sex differences in heart failure with preserved ejection fraction', *Journal of the American Heart Association*, 10(5), pp. 1–20. Available at: https://doi.org/10.1161/JAHA.120.018574.

Speir, M.L. *et al.* (2021) 'UCSC Cell Browser: visualize your single-cell data', *Bioinformatics*. Edited by C. Kendziorski, 37(23), pp. 4578–4580. Available at: https://doi.org/10.1093/bioinformatics/btab503.

Tucker, N.R. *et al.* (2020) 'Transcriptional and Cellular Diversity of the Human Heart', *Circulation*, 142(5), pp. 466–482. Available at: https://doi.org/10.1161/CIRCULATIONAHA.119.045401.

Vignier, N. *et al.* (2009) 'Nonsense-mediated mrna decay and ubiquitin-proteasome system regulate cardiac myosin-binding protein c mutant levels in cardiomyopathic mice', *Circulation Research*, 105(3), pp. 239–248. Available at: https://doi.org/10.1161/CIRCRESAHA.109.201251.

Waldman, M. *et al.* (2018) 'Alstrom syndrome: Renal findings in correlation with obesity, insulin resistance, dyslipidemia and cardiomyopathy in 38 patients prospectively evaluated at the NIH clinical center', *Mol Genet Metab*. 2018/08/02, 125(1–2), pp. 181–191. Available at: https://doi.org/10.1016/j.ymgme.2018.07.010.

Walkin, L. *et al.* (2013) 'The role of mouse strain differences in the susceptibility to fibrosis: A systematic review', *Fibrogenesis and Tissue Repair*, 6(1), pp. 1–12. Available at: https://doi.org/10.1186/1755-1536-6-18.

Figures and Tables

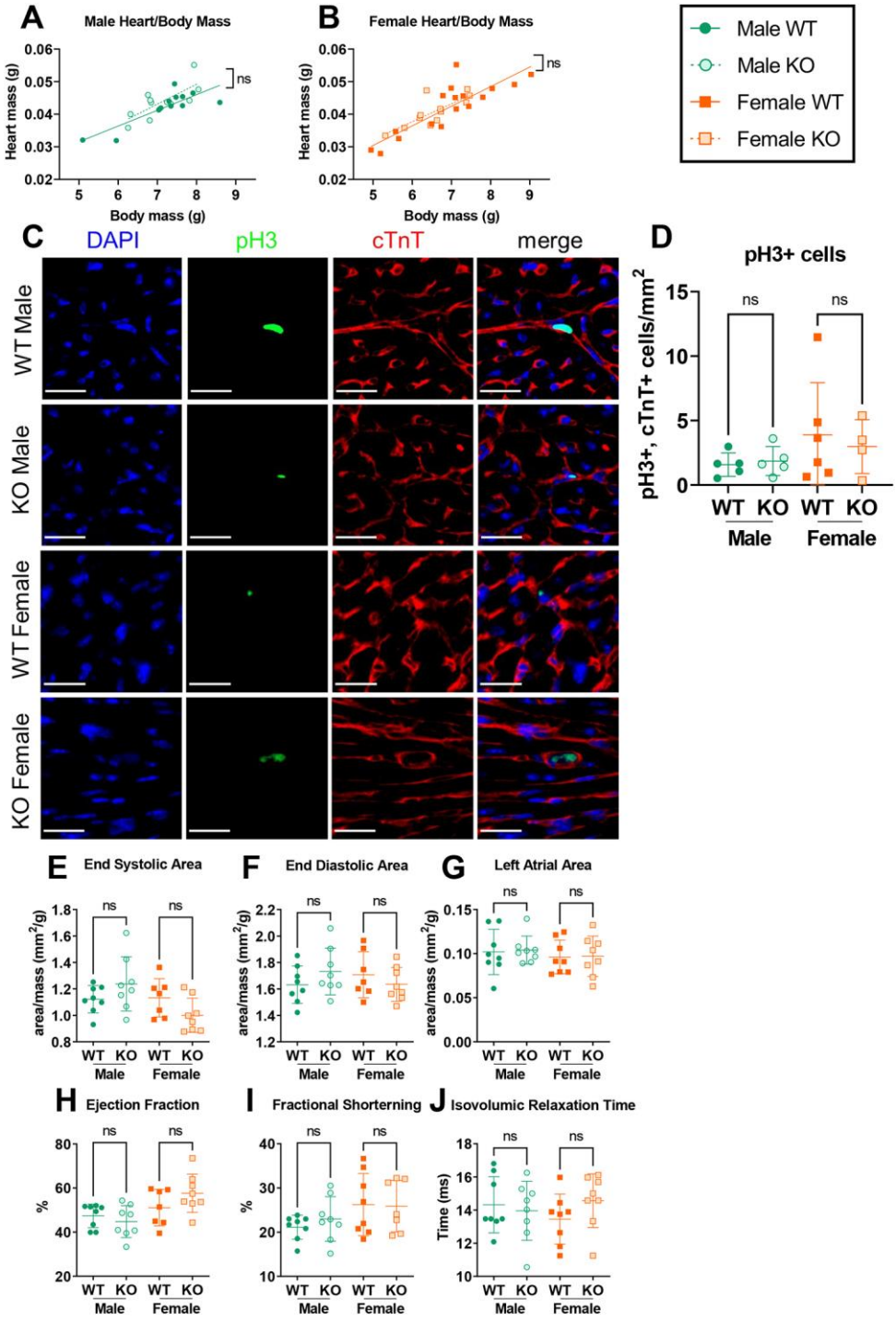

Fig. 1. Neither male nor female global *Alms1* knockout mice exhibit a cardiac phenotype at post-natal day 15. (**A,B**) Linear regression of heart and body mass for males and females respectively. (**C**) Representative images of immunofluorescent staining of cardiac left ventricle for proliferative marker phosphorylated histone H3 (pH3) with co-staining for cardiac troponin (cTnT) and DAPI. Scale bars 20µm. (**D**) Quantification of (**C**). (**E-J**)

Echocardiography data. Area values calculated from echocardiography (**E-G**) are normalised to total body mass. Each data point represents an individual animal with bars in (**D-J**) representing mean ± sd. Comparison between groups in (**D-J**) was undertaken using two-way ANOVA with Tukey's multiple comparisons test. Lines in linear regression graphs (**A,B**) represent lines of best fit. Comparisons between lines of best fit was undertaken by simple linear regression, with square brackets showing comparison of y intercepts. No significant change was seen between gradients. For (**A,B**) N = 13, 11, 17 and 12 for WT males, KO males, WT females and KO females respectively. For (**D**) N = 5, 5, 6 and 4 for WT males, KO males, WT females and KO females respectively. For (**E-J**) N = 8, 8, 7 and 8 for WT males, KO males, WT females and KO females respectively.

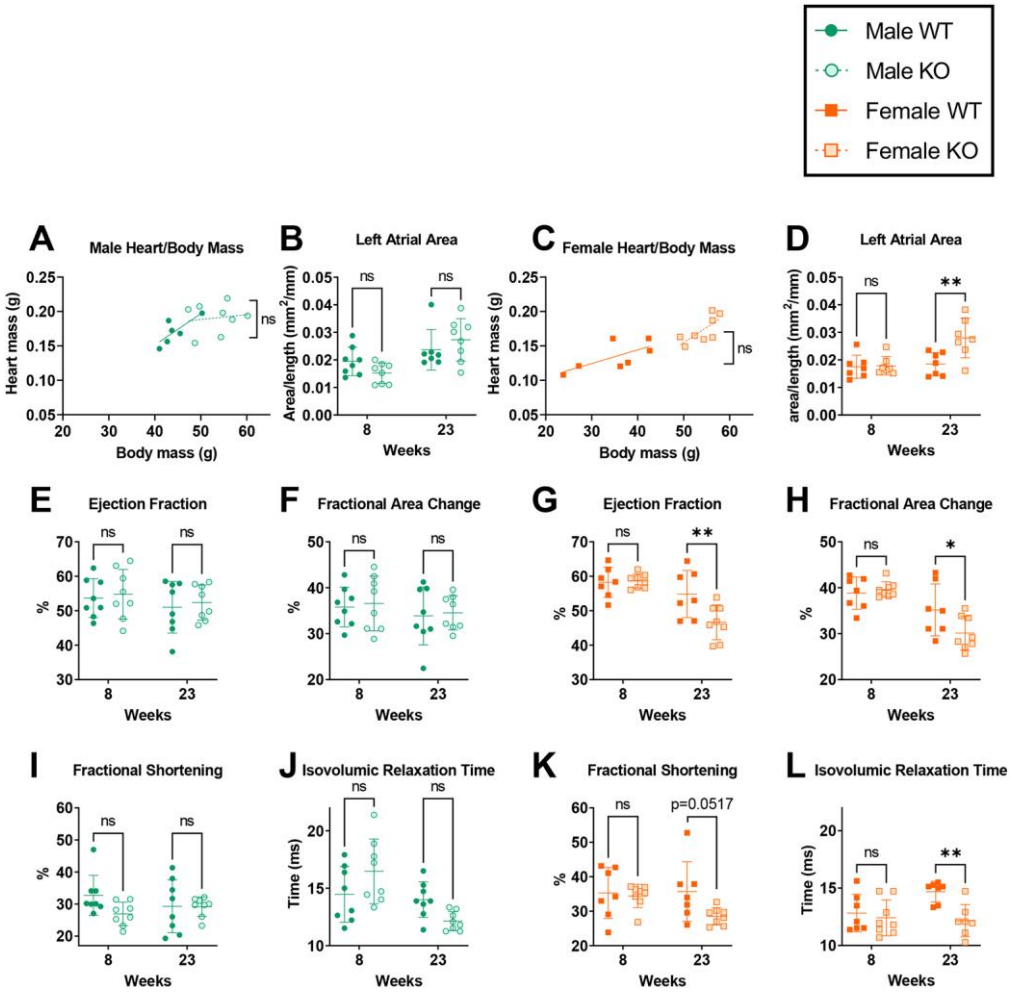

Fig. 2. Systolic and diastolic dysfunction develops in female but not male global *Alms1* knockout mice with age. Linear regression of heart to body mass of males (**A**) and females (**C**) at 24 weeks of age. (**B, D-L**) Echocardiography parameters of male and female mice at 8 and 23 weeks of age. Each data point represents an individual animal. Left atrial area values (**B,D**) are normalised to nose-anus length. Bars in (**B, D-L**) representing mean ± standard deviation. Lines in linear regression graphs (**A,C**) represent lines of best fit. Comparison between groups (**B, D-L**) was undertaken using a two-way ANOVA with Šídák's multiple comparisons test. Comparisons between lines of best fit (**A,C**) were undertaken by simple linear regression, with square brackets showing comparison of y intercepts. No significant change was seen between gradients. * denotes $p<0.05$, ** denotes $p<0.01$ and **** denotes $p<0.0001$. N = 8, 8, 7 and 8 for WT males, KO males, WT females and KO females respectively

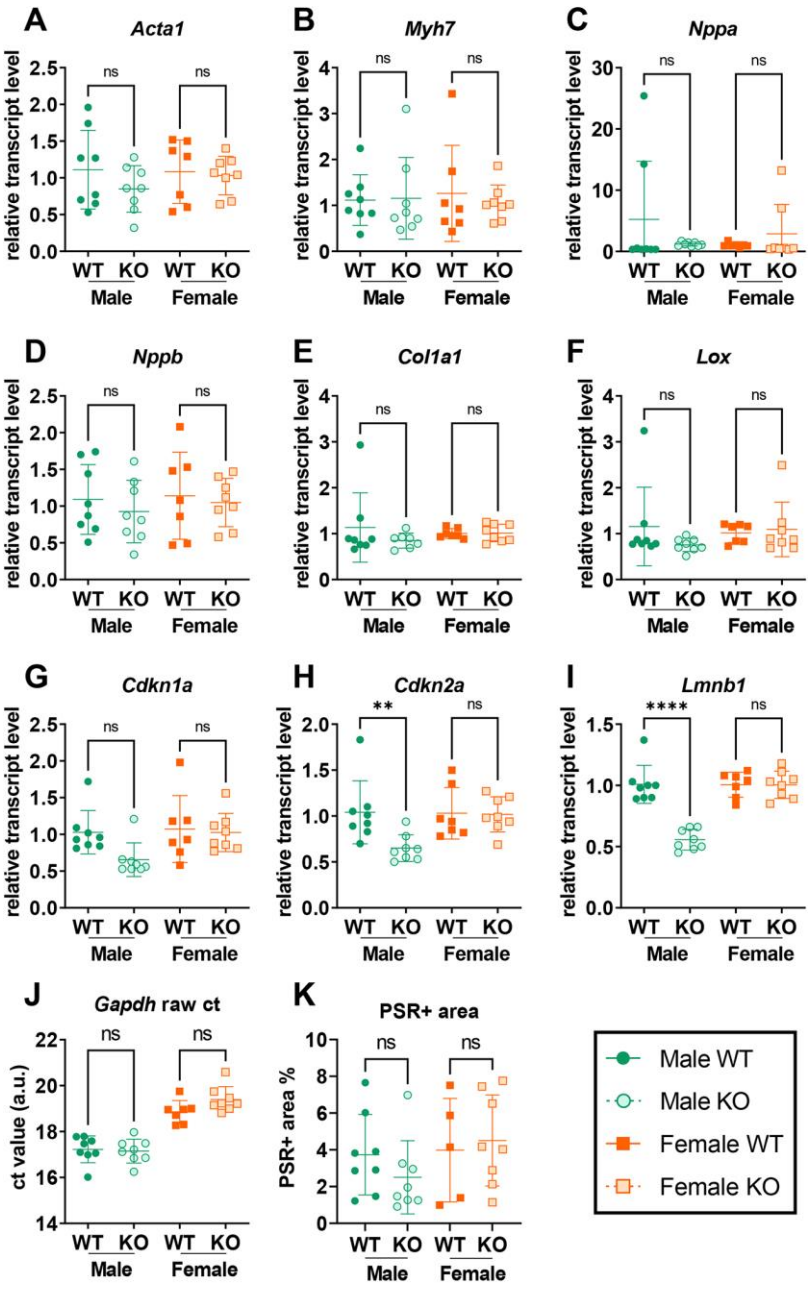

Fig. 3. No transcriptional nor histological correlates for echocardiography phenotype of global *Alms1* knockout. (**A-I**) Transcriptional analysis of hearts at 24 weeks old. Data presents ct values normalised to G*apdh* run in duplex. (**J**) An example of raw *Gapdh* ct values from duplexed reactions. (**K**) Quantification of picrosirius red (PSR) staining by pixel thresholding. Samples analysed from 24 week old male and female *Alms1* knockout mice. Each data point represents an individual animal, with bars representing mean ± sd. Comparison between groups performed using a two-way ANOVA with Tukey's multiple comparisons test. ** denotes $p<0.01$. N = 8, 8, 7 and 8 for WT males, KO males, WT females and KO females respectively.

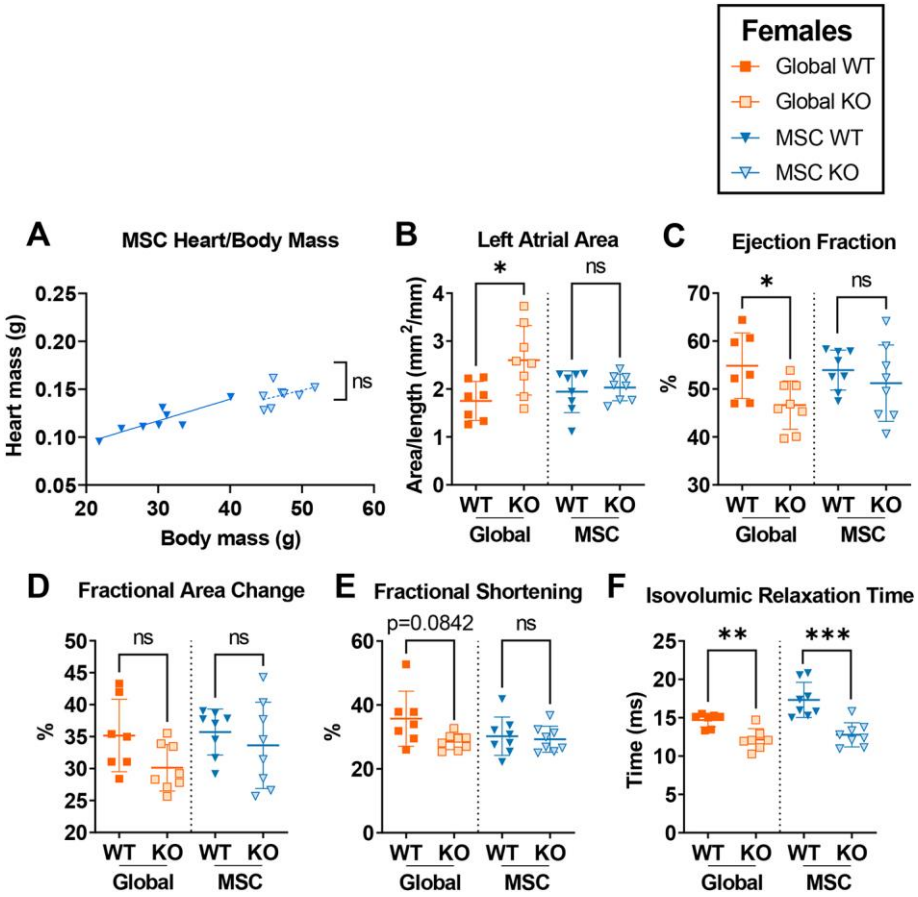

Fig. 4. Mesenchymal stem cell-specific *Alms1* knockout in female mice does not recapitulate the phenotype of global *Alms1* knockout. All global knockout (KO) data are repeated from figure 2 for comparison to mesenchymal stem cell- (MSC-) specific *Alms1* KO. **(A)** Linear regression of heart to body mass at 24 weeks of age (**B-F**) Data obtained from analysis of echocardiography performed at 23 weeks of age. Left atrial area (**B**) normalised to nose-anus length. Each data point represents an individual animal with bars in (**B-F**) representing mean ± sd. Lines in linear regression graph (**A**) represent lines of best fit. Global WT/KO and MSC WT/KO experiments were performed with identical design at different times; this is reflected in the dotted line separating the two cohorts. Comparison between WT and KO in (**B-F**) was undertaken using an unpaired two-tailed Student's t-test followed by a Bonferroni correction for multiple testing. Comparisons between lines of best fit (**A**) was undertaken using simple linear regression, with square brackets showing comparison of y intercepts. No significant change was seen between gradients. * denotes $p<0.05$, ** denotes $p<0.01$ and *** denotes $p<0.001$. N = 7, 8, 8 and 8 for global WT, global KO, MSC WT and MSC KO respectively.

Table 1. Comparison of Current and Previous *Alms1* knockout mouse models.

Abbreviations: bp, basepairs; ENU, N-ethyl-N-nitrosourea; ES cell, embryonic stem cell; GKO, global knockout; HFD, high-fat diet; MSC KO, MSC-specifical Alms1 knockout; p15.5, postnatal day 15.5; WT, wild-type.

Mouse model	**Alms1$^{GT/GT}$**	**Alms1$^{foz/foz}$ (fat aussie)**	**Alms1^{L2131X}**	**Alms1$^{flin/flin}$** and **Alms$^{flin/flin}$; Adipo-Cre$^{+/-}$**	**Alms1 GKO** and **Alms1 MSC KO**
Generation method	Gene trap in intron 13 (Collin *et al.*, 2005)	Spontaneous 11 bp deletion in exon 8 (T Arsov *et al.*, 2006)	ENU-induced; nonsense mutation in exon 10 (Li *et al.*, 2007)	Alms1$^{(EUCOMM)tm1e}$ (Geberhiwot *et al.*, 2021)	Alms1$^{(EUCOMM)tm1c}$ and Alms1$^{(EUCOMM)tm1d}$ (McKay *et al.*, 2023)
Alms1 KO validation method	qPCR for *Alms1* and SDS-PAGE of PCR amplicons (Collin *et al.*, 2005)	cDNA sequencing and SDS-PAGE of PCR amplicons (T Arsov *et al.*, 2006)	cDNA sequencing (Li *et al.*, 2007)	qPCR for *Alms1* and SDS-PAGE of PCR amplicons (Geberhiwot *et al.*, 2021)	qPCR for *Alms1* and SDS-PAGE of PCR amplicons (McKay *et al.*, 2023)
Mouse back-ground	Gene trap in 129 ES cell. Mice then backcrossed onto C57BL/6J for 1 generation (Collin *et al.*, 2005), and later for 10 more generations (Jagger *et al.*, 2011). Also	NOD/B10 background (Todor Arsov, Silva, *et al.*, 2006). Also backcrossed onto BALB/c and C57BL6/J (Farrell *et al.*, 2014).	Mixed C57Bl6/NOD genetic background (Li *et al.*, 2007)	C57Bl6/N (Geberhiwot *et al.*, 2021)	C57Bl6/N (McKay *et al.*, 2023)

	crossed onto C57BL6/Ei background (Favaretto *et al.*, 2014).				
First published	2005 (Collin *et al.*, 2005)	2006 (Todor Arsov, Silva, *et al.*, 2006)	2007 (Li *et al.*, 2007)	2020 (Geberhiwot *et al.*, 2021)	This publication
Sexes studied	Both	Both	Both	Males only (Geberhiwot *et al.*, 2021)	Both (McKay *et al.*, 2023)
Heterozygous phenotype	Same as WT (Collin *et al.*, 2005)	Same as WT (Todor Arsov, Silva, *et al.*, 2006)	Same as WT (Li *et al.*, 2007)	Not reported	Not studied
Diet	Chow (Collin *et al.*, 2005; Favaretto *et al.*, 2014)	Chow and HFD (Todor Arsov, Silva, *et al.*, 2006)	Not reported (Li *et al.*, 2007)	Chow (Geberhiwot *et al.*, 2021)	45% fat diet (McKay *et al.*, 2023)
Appetite	Not reported	Hyperphagia from 60 days of age (Todor Arsov, Silva, *et al.*, 2006)	Not reported	Not reported	Hyperphagia (McKay *et al.*, 2023)
Body weight	Obese. Divergence in body weight from WT at 8-12 weeks of age (Collin *et al.*, 2005; Favaretto *et al.*, 2014)	Body mass increased (Todor Arsov, Silva, *et al.*, 2006); Obese, divergence around 12 weeks of age (Larter *et al.*, 2009)	Greater body weight than WT. Divergence from WT at 7-10 weeks of age (Li *et al.*, 2007)	Greater body weight at 3 months of age in Alms1$^{flin/flin}$ (Geberhiwot *et al.*, 2021)	Greater body weight than WT from 10-12 weeks (McKay *et al.*, 2023)

Fat mass	Fat pads heavier than WT (Collin *et al.*, 2005; Favaretto *et al.*, 2014). Enlarged adipocyte size/hypertrophy (Favaretto *et al.*, 2014).	Higher percentage fat mass and heavier adipose depots (Larter *et al.*, 2009, 2012).	Greater than WT. Hypertrophy of adipose tissue seen (Li *et al.*, 2007).	Not reported	Higher body fat mass from 10 weeks and heavier fat pads at 24 weeks (McKay *et al.*, 2023)
Lean mass	Not reported	Increased lean mass at 250 days of age (Todor Arsov, Silva, *et al.*, 2006)	Same as WT (Li *et al.*, 2007)	Not reported	Same as WT (McKay *et al.*, 2023)
Fasting blood glucose	Males hyperglycaemic from 16 weeks (Collin *et al.*, 2005)	Hyperglycaemia in older mice (Todor Arsov, Silva, *et al.*, 2006)	Same as WT (Li *et al.*, 2007)	Alms1$^{flin/flin}$ hyperglycaemic at 3 months (Geberhiwot *et al.*, 2021)	Mild hyperglycaemia (McKay *et al.*, 2023)
Serum insulin	Hyperinsulinemia (Collin *et al.*, 2005; Favaretto *et al.*, 2014)	Hyperinsulinaemia (preceeding hyperglycaemia) (Todor Arsov, Silva, *et al.*, 2006; Larter *et al.*, 2009)	Hyperinsulinaemia (Li *et al.*, 2007)	Not reported	Hyperinsulinaemia (preceeding hyperglycaemia) (McKay *et al.*, 2023)
Serum triglyceride	Same as WT (Collin *et al.*, 2005; Favaretto *et*	Same as WT (Todor Arsov, Silva, *et al.*, 2006; Larter *et*	Elevated (Li *et al.*, 2007)	Not reported	Same as WT (McKay *et al.*, 2023)

	al., 2014)	*al.*, 2009)			
Serum cholesterol	Elevated (Collin *et al.*, 2005; Favaretto *et al.*, 2014)	Elevated (Todor Arsov, Silva, *et al.*, 2006; Larter *et al.*, 2009)	Elevated (Li *et al.*, 2007)	Not reported	Elevated (McKay *et al.*, 2023)
Brown fat	Not reported	Heavier BAT with higher fat content, lower mitochondrial density (Poekes *et al.*, 2017)	Higher lipid content in iBAT (Li *et al.*, 2007)	Not reported	Heavier BAT due to increased lipid content in females but not males (McKay *et al.*, 2023)
Liver	Hepato-megaly and steatosis (Collin *et al.*, 2005)	Enlarged and steatotic (Todor Arsov, Silva, *et al.*, 2006); steatohepatitis on HFD (Todor Arsov, Larter, *et al.*, 2006)	Steatosis (Li *et al.*, 2007)	Not reported	Hepatomegaly and steatosis in both GKO and MSC KO (McKay *et al.*, 2023)
Kidney	Enlarged & heavier; dilated proximal tubules (Collin *et al.*, 2005)	Not reported	Dilated tubules in cortex (Li *et al.*, 2007)	Not reported	Enlarged & heavier (data not published)
Pancreas	Not reported	Islet hyperplasia (Todor Arsov, Silva, *et al.*, 2006)	Not reported	Not reported	Not investigated
Vision	Impaired	Impaired;	Defective	Not reported	Not

	(Collin *et al.*, 2005)	degeneration with age (Brun *et al.*, 2019)	rhodopsin transport in retina (Li *et al.*, 2007)		investigated
Hearing	Impaired (Collin *et al.*, 2005; Jagger *et al.*, 2011)	Impaired (Todor Arsov, Silva, *et al.*, 2006)	Not reported	Not reported	Not investigated
Fertility	Hypogonadism in males: atrophic seminiferous tubules, no sperm heads (Collin *et al.*, 2005)	Males infertile; testes smaller; decreased germ cells; dysfunctional sperm (Todor Arsov, Silva, *et al.*, 2006)	Reduced germinal cells in testis; reduced numbers and shorter sperm flagella (Li *et al.*, 2007)	Not reported	Not investigated
Heart	P15.5 hearts greater size, larger cardiomyocytes and markers of proliferation detected (Shenje *et al.*, 2014)	Not reported	Not reported	Not reported	No change detected at p15.5. Evidence of restrictive cardiomyopathy at 23 weeks of age in females but not males.

Table 2. Reagents used for immunohistochemistry.

Item	Catalogue No.	Company
Bond Epitope Retrieval ER1 Solution	AR9961	Leica Biosystems
Bond Epitope Retrieval ER2 Solution	AR9640	Leica Biosystems
Bond Wash Solution	AR9590	Leica Biosystems
Bond Polymer Refine Detection Kit	DS9800	Leica Biosystems
Normal Goat Serum	ab7481	Abcam
Mouse on Mouse Polymer IHC Kit	ab269452	Abcam
Rhodamine-conjugated Wheat Germ Agglutinin	RL-1022	Vector Laboratories
DAPI	D3571	Life Technologies
520 Green Opal reagent pack	FP1487001KT	Akoya
650 Blue opal reagent pack	FP1496001KT	Akoya

Table 3. Antibodies used for immunohistochemistry.

Antibody	**Catalog No.**	**Species raised in**	**Company**	**Dilution**
anti-cTnT (cardiac troponin)	MA512960	Mouse	Invitrogen, USA	1:500
Anti-Histone H3 (phospho S10)	ab5176	Rabbit	Abcam, UK	1:400
Goat F(ab) Anti-Rabbit IgG H&L (HRP)	ab7171	Goat	Abcam, UK	1:500

Table 4. TaqMan primer/probe mixes.

Reagent	**Gene target**	**Taqman Probe ID**	**Catalog No.**
Mouse GAPD (GAPDH) Endogenous Control (VIC™/MGB probe, primer limited)	*Gapdh*	Mm99999915_g1	4352339E
TaqMan™ Gene Expression Assay (FAM)	*Alms1* exon 6-7	Mm01189441_m1	4351372
TaqMan™ Gene Expression Assay (FAM)	*Acta1*	Mm00808218_g1	4331182
TaqMan™ Gene Expression Assay (FAM)	*Myh7*	Mm00600555_m1	4331182
TaqMan™ Gene Expression Assay (FAM)	*Nppa*	Mm01255748_g1	4331182
TaqMan™ Gene Expression Assay (FAM)	*Nppb*	Mm01255770_g1	4331182
TaqMan™ Gene Expression Assay (FAM)	*Col1a1*	Mm00801666_g1	4331182
TaqMan™ Gene Expression Assay (FAM)	*Lox*	Mm00495386_m1	4331182
TaqMan™ Gene Expression Assay (FAM)	*Cdkn1a*	Mm04205640_g1	4331182
TaqMan™ Gene Expression Assay (FAM)	*Cdkn2a*	Mm00494449_m1	4331182
TaqMan™ Gene Expression Assay (FAM)	*Lmnb1*	Mm00521949_m1	4331182

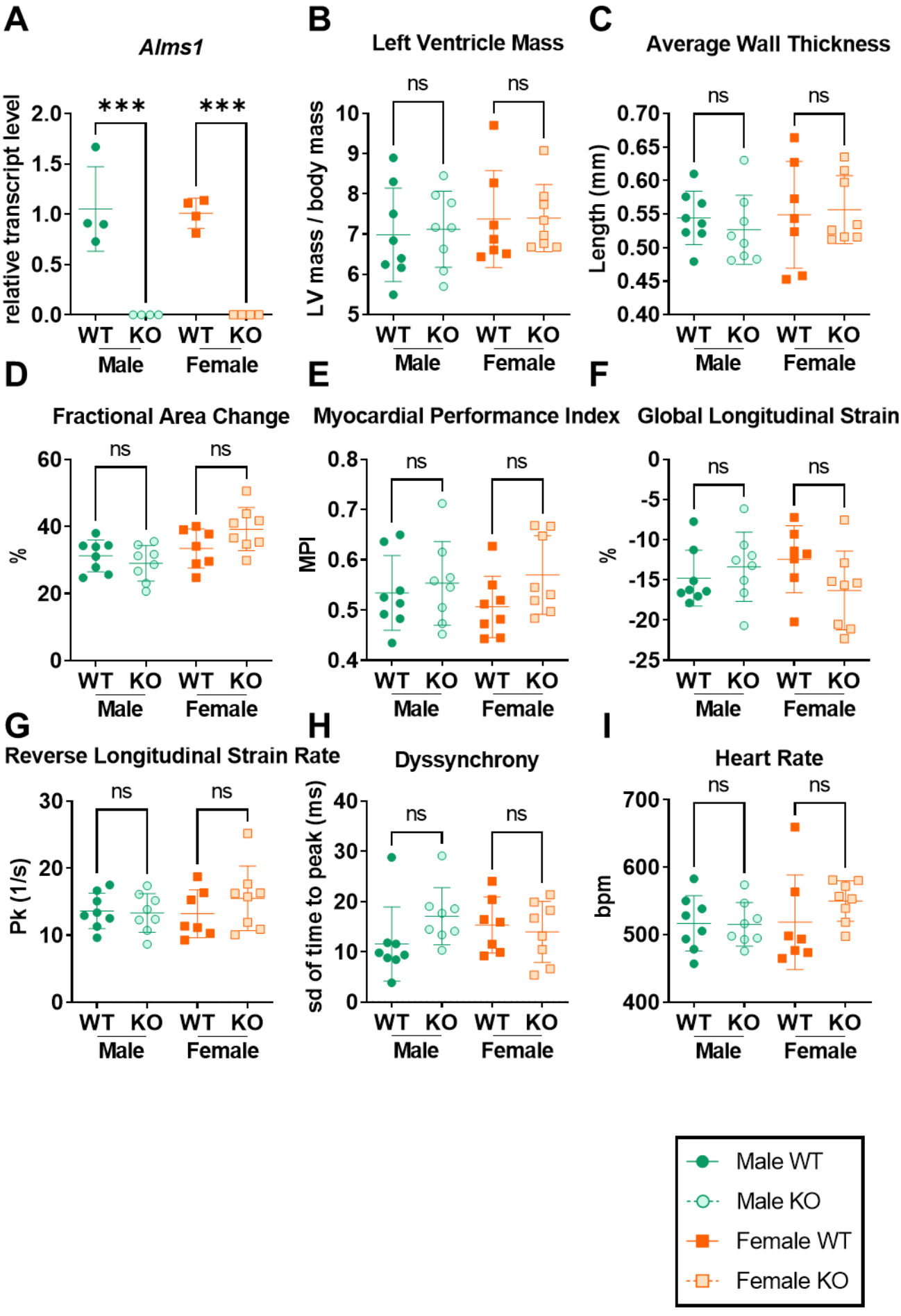

Fig. S1. Neither male nor female global *Alms1* knockout mice exhibit an echocardiographic phenotype at post-natal day 15. (**A**) qPCR confirmation of *Alms1* loss in heart tissue of global *Alms1* knockout (KO) mice with a Taqman probe for the 6-7 exon junction of *Alms1* **(B-I)** Echocardiography data. Left ventricle mass values (**B**) are normalised to total body mass. (**A**) Data presents ct values normalised to *Gapdh* run in duplex. Each data point represents an individual animal with bars representing mean ± sd. Comparison between groups in performed using two-way ANOVA with Tukey's multiple comparisons test. For (**A**) N = 4/group. For (**B-I**) N = 8, 8, 7 and 8 for WT males, KO males, WT females and KO females respectively.

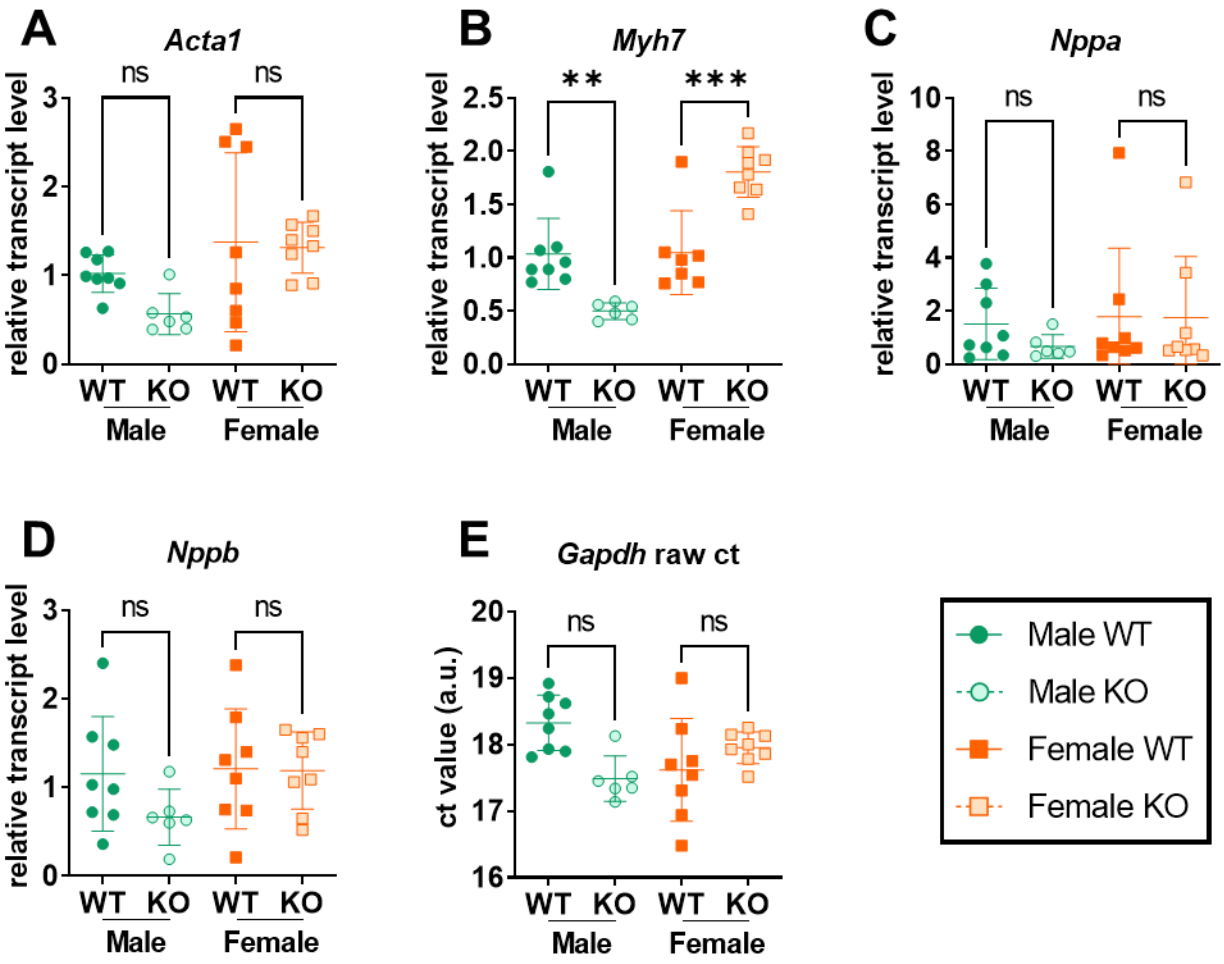

Fig. S2. Neither male nor female global *Alms1* knockout mice exhibit a cardiac transcriptional phenotype at post-natal day 15. (**A-D**) qPCR evaluation of heart tissue for typical markers of cardiomyopathy. Data presents ct values normalised to *Gapdh* run in duplex. (**E**) An example of raw *Gapdh* ct values from duplexed reactions. Each data point represents an individual animal with bars representing mean ± sd. Comparison between groups in performed using two-way ANOVA with Tukey's multiple comparisons test. N = 8, 8, 7 and 8 for WT males, KO males, WT females and KO females respectively.

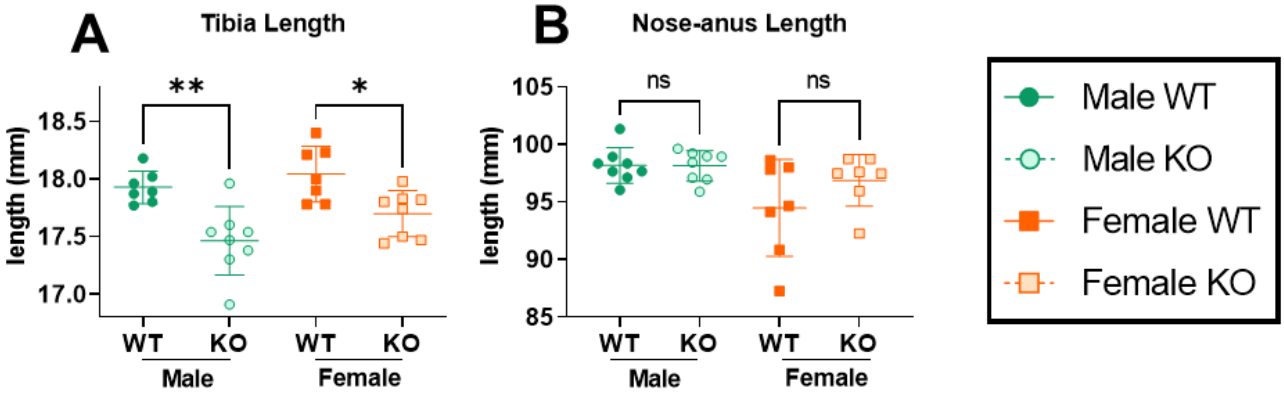

Fig. S3. Evaluation of parameters for normalisation of echocardiography area and mass values in adult global *Alms1* knockout mice. (**A**) Tibia length measured following cull at 24 weeks. (**B**) Nose-anus length measured in anaesthetised animals immediately following echo at 23 weeks. Each data point represents an individual animal with bars representing mean ± sd. Comparison between groups performed using two-way ANOVA with Tukey's multiple comparisons test. * denotes $p<0.05$ and ** denotes $p<0.01$. N = 8, 8, 7 and 8 for WT males, KO males, WT females and KO females respectively

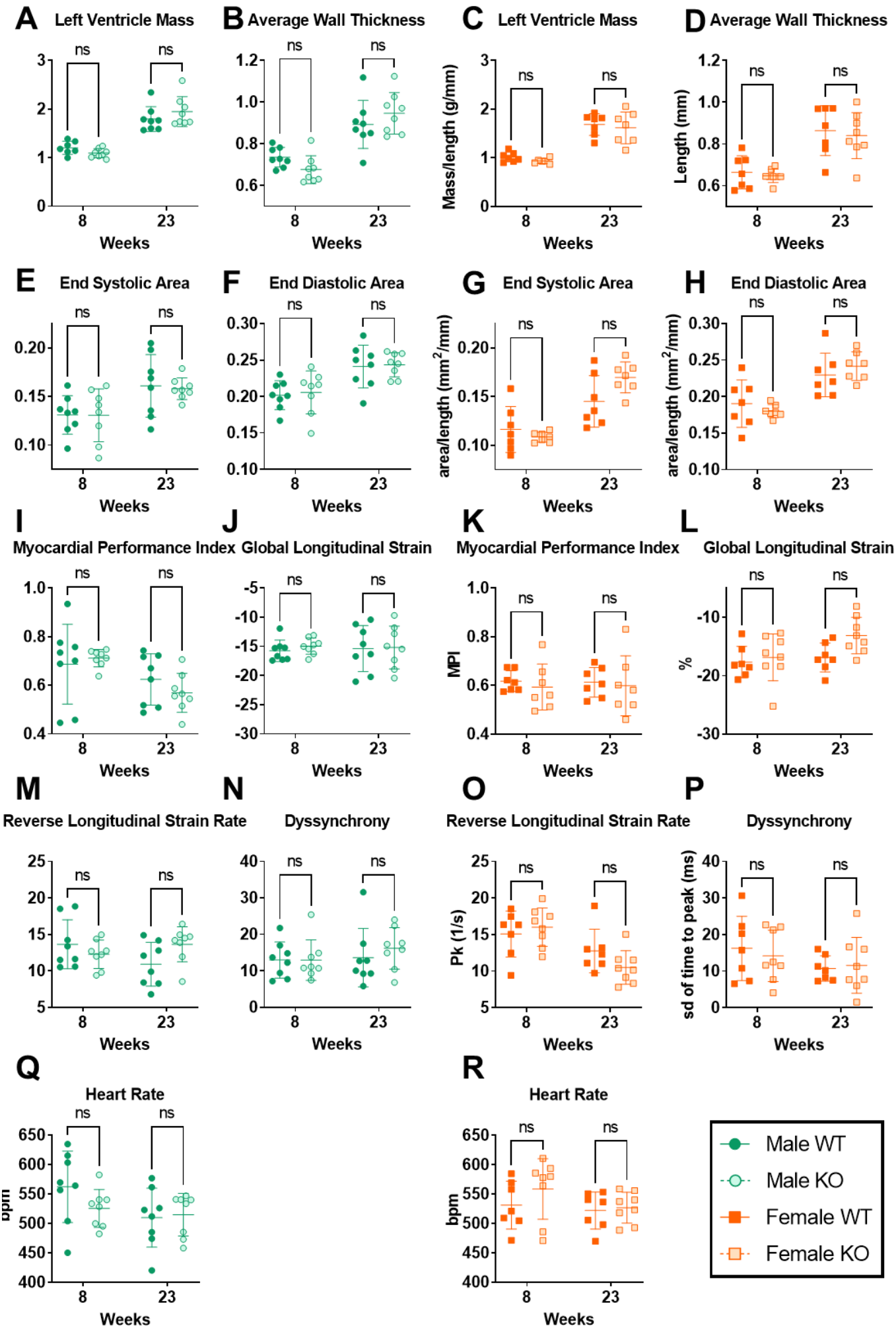

Fig. S4. Systolic and diastolic dysfunction develops in female but not male global *Alms1* knockout mice with age. Echocardiography parameters measured at 8 and 23 weeks of age. Left ventricle mass and area values (**A,C,E-H**) are normalised to nose-anus length. Each data point represents an individual animal with bars representing mean ± sd. Comparison between groups performed using a two-way ANOVA with Šídák's multiple comparisons test. * denotes $p<0.05$ and ** denotes $p<0.01$. N = 8, 8, 7 and 8 for WT males, KO males, WT females and KO females respectively.

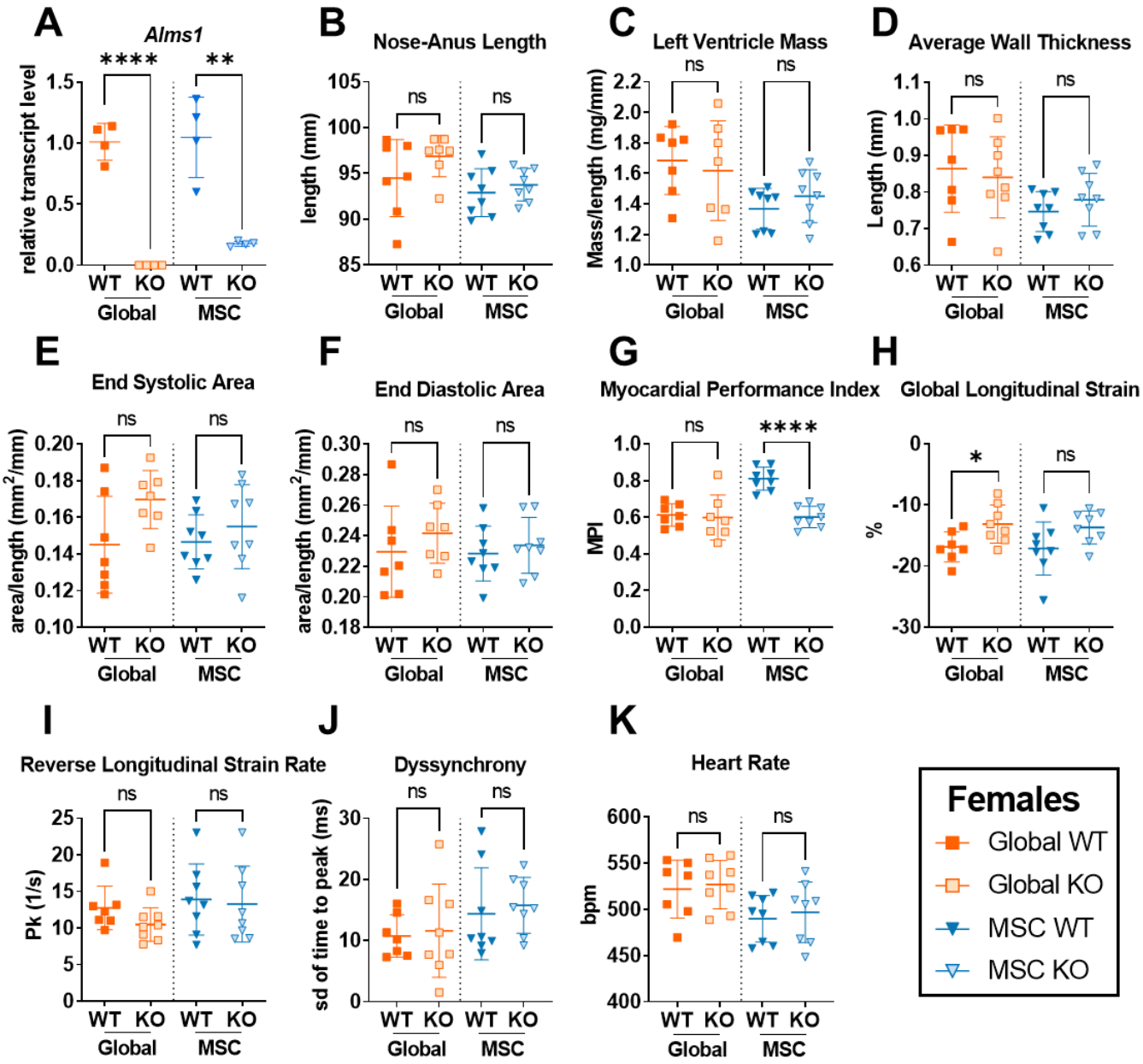

Fig. S5. Mesenchymal stem cell-specific *Alms1* knockout does not recapitulate the phenotype of global *Alms1* knockout. All global KO data repeated from Figure 2 and Fig. S4 for comparison to MSC-specific *Alms1* KO. (**A**) qPCR confirmation of partial *Alms1* loss in heart tissue of MSC-specific Alms1 KO mice with a Taqman probe for the 6-7 exon junction of *Alms1*. (**B**) Nose to anus length of females at 23 weeks of age. (**C-K**) Data obtained from analysis of echocardiography performed on female animals at 23 weeks of age. Mass and area values (**C,E,F**) normalised to nose-anus length. Each data point represents an individual animal with bars representing mean ± sd. Global WT/KO and MSC WT/KO experiments were

performed with identical design at different times; this is reflected in the dotted line separating the two cohorts. Comparison between WT and KO was performed using an unpaired two-tailed Student's t-test followed by a Bonferroni correction for multiple testing. * denotes $p<0.05$, ** denotes $p<0.01$, *** denotes $p<0.001$ and **** denotes $p<0.0001$. (**A**) N = 4/group (**B-K**) N = 7, 8, 8 and 8 for female global WT, global KO, MSC WT and MSC KO respectively.

Supplementary Materials and Methods

Electrocardiographic analysis

Analysis of echocardiographic data was performed using Visualsonics Vevo LAB 5.71 software (FUJIFILM VisualSonics). End systolic and end diastolic area, ejection fraction, fractional area change, left ventricle mass and average wall thickness were calculated from the PSLA EKV. End systolic and end diastolic area and ejection fraction were calculated using the automated artificial-intelligence software AutoLV [1]. Fractional area change, left ventricle mass and average wall thickness were calculated after manual tracing of the contours of PSLA epicardial and endocardial area and axis length at systole and diastole, as indicated by AutoLV. Fractional shortening was calculated from M-mode images using AutoLV. Modified right side PSLA EKV was used to manually measure left atrium area, choosing the time frame immediately after the mitral valve closure. Isovolumic relaxation time (IVRT), isovolumic relaxation time (IVCT) and ejection time (ET) were all calculated by manual analysis of Doppler; three consecutive annotations for each index were made. IVRT measures the time between aortic valve closing and the mitral valve opening. Myocardial performance index (MPI) was calculated as the sum of IVRT and IVCT divided by ET. Finally, the 'Vevo Strain' function of the Vevo LAB software was used to analyse PSLA EKV, generating values for global longitudinal strain (GLS), reverse longitudinal strain rate (rLSR) and ventricular dyssynchrony. Ventricular dyssychrony was calculated as the standard deviation of strain across the 6 panels generated by 'Vevo Strain'.

Tissue studies

Mice were culled by cervical dislocation under isoflurane anaesthesia. Dissected hearts were rinsed in phosphate-buffered saline (PBS), and weighed after blotting of excess fluid. Whole neonatal hearts were fixed in 4% paraformaldehyde or snap-frozen in liquid nitrogen. The bottom 1/5th (apex) of adult hearts was fixed in 4% PFA, and the middle 2/5ths (ventricles) snap-frozen in liquid nitrogen. Adult tibia were also collected.

For histological analysis, fixed cardiac tissue was paraffin-embedded and 5µm sections cut. For picrosirius red (PSR) staining slides were dewaxed in xylene, rehydrated in decreasing concentrations of ethanol and washed in water before incubation in direct red picric acid solution for 2 hours, washing, dehydrating in ethanol, clearing in xylene, and mounting. Immunofluorescence staining of neonatal heart sections was performed using the Leica BOND III immunostainer robot at room temperature, with reagents detailed in **Table S1**. Sequential staining for histone H3, cardiac troponin

(cTnT) and wheat germ agglutinin (WGA) was performed, with antibodies and conditions used detailed in **Table S2**. Washing with TBS-T buffer (composition) was performed between steps. For histone H3, antigen retrieval was by incubation in Bond Epitope Retrieval ER1 Solution (Leica Microsystems) for 20 minutes before peroxide blocking, blocking in diluted goat serum diluted 1:5 for 10 minutes. Anti-histone H3 antibody was incubated for 60 minutes before incubation with Goat Anti-Rabbit IgG HRP-conjugated secondary antibody for 30 minutes. Finally tyramide signal amplification was performed with addition of tyramide substrate FITC green opal 520. Next cTnT staining was performed. Firstly antigen retrieval was performed by incubation in Bond Epitope Retrieval ER1 Solution for 10 minutes. Peroxide blocking was performed for 10 minutes followed by serum blocking for 10 minutes using blocking solution from the Mouse on Mouse Polymer IHC Kit (Abcam). Incubation of anti-cTnT was performed for 60 minutes before addition of secondary polymer from the Mouse on Mouse Polymer IHC Kit (Abcam) for 30 minutes. Finally, the tyramide substrate blue CY5 opal 650 was added. Next WGA staining was performed. Antigen retrieval was performed by incubation in Bond Epitope Retrieval ER1 Solution for 10 minutes. Peroxide blocking was then performed for 10 minutes before serum blocking in goat serum diluted 1:5 for 10 minutes. Rhodamine-conjugated WGA diluted 1:75 was then incubated for 60 minutes. Finally nuclear counter-staining was performed by incubation with DAPI, diluted 1:1000. All histological slides were imaged using a Zeiss Axioscan.Z1 with Zen2.6 software.

Gene expression analysis

RNA was extracted from snap-frozen heart tissue using the Qiagen RNeasy Fibrous Tissue Mini Kit after homogenisation in 2mL tubes containing 2.8mm ceramic beads stored on dry ice, using the Omni Bead Ruptor 24 Elite with the pre chilled Omni Cryo unit filled with dry ice. 10µL of RLT buffer was added per 1mg of heart tissue. 300µL homogenate was used for RNA extraction. After elution, RNA concentration was measured using the NanoDrop ONE before dilution to 100ng/µL in nuclease-free water. Reverse transcription was performed using the High Capacity cDNA Reverse Transcription Kit (Applied Biosystems) in the Eppendorf Mastercycler X50s, using 1000ng per reaction. cDNA solution was then diluted 1 in 4 with nuclease-free water. Control reactions without reverse transcriptase were performed alongside all experimental reactions.

Real-time quantitative PCR (RT-qPCR) was performed using TaqMan reagents on a LightCycler® 480 Instrument II (Roche) in duplex with minor groove binder (MGB) probes [2]. *Gapdh* was evaluated as a housekeeping control gene for normalisation using a 2'-chloro-7'phenyl-1,4-dichloro-6-carboxy-fluorescein (VIC)-coupled probe. Primer efficiency was calculated by dilution standard curve prior to

experimental reactions. All reactions were run in triplicate, and RT- and non-template controls were run on the same plate. Crossing point (Cp) values were calculated using LightCycler 480 software using the Abs quant / 2nd derivative max function. Cp values for the gene of interest were normalised to duplexed *Gapdh* Cp values after adjusting for primer efficiency, as first described by Pfaffl [3]. Raw Cp values for the gene of interest and *Gapdh* were also visualised in all cases (e.g. **Figure 3J, S2E**). Taqman primer and probe mixes used for qPCR were purchased from Life Technologies and are listed in **Table S3**.

Table S1. Reagents used for immunohistochemistry.

Item	Catalog No.	Company
Bond Epitope Retrieval ER1 Solution	AR9961	Leica Biosystems
Bond Epitope Retrieval ER2 Solution	AR9640	Leica Biosystems
Bond Wash Solution	AR9590	Leica Biosystems
Bond Polymer Refine Detection Kit	DS9800	Leica Biosystems
Normal Goat Serum	ab7481	Abcam
Mouse on Mouse Polymer IHC Kit	ab269452	Abcam
Rhodamine-conjugated Wheat Germ Agglutinin	RL-1022	Vector Laboratories
DAPI	D3571	Life Technologies
520 Green Opal reagent pack	FP1487001KT	Akoya
650 Blue opal reagent pack	FP1496001KT	Akoya

Table S2. Antibodies used for immunohistochemistry.

Antibody	Catalog No.	Species raised in	Company	Dilution
anti-cTnT (cardiac troponin)	MA512960	Mouse	Invitrogen, USA	1:500
Anti-Histone H3 (phospho S10)	ab5176	Rabbit	Abcam, UK	1:400
Goat F(ab) Anti-Rabbit IgG H&L (HRP)	ab7171	Goat	Abcam, UK	1:500

Table S3. TaqMan primer/probe mixes.

Reagent	Gene target	Taqman Probe ID	Catalog No.
Mouse GAPD (GAPDH) Endogenous Control (VIC™/MGB probe, primer limited)	*Gapdh*	Mm99999915_g1	4352339E
TaqMan™ Gene Expression Assay (FAM)	*Alms1* exon 6-7	Mm01189441_m1	4351372
TaqMan™ Gene Expression Assay (FAM)	*Acta1*	Mm00808218_g1	4331182
TaqMan™ Gene Expression Assay (FAM)	*Myh7*	Mm00600555_m1	4331182
TaqMan™ Gene Expression Assay (FAM)	*Nppa*	Mm01255748_g1	4331182
TaqMan™ Gene Expression Assay (FAM)	*Nppb*	Mm01255770_g1	4331182
TaqMan™ Gene Expression Assay (FAM)	*Col1a1*	Mm00801666_g1	4331182
TaqMan™ Gene Expression Assay (FAM)	*Lox*	Mm00495386_m1	4331182
TaqMan™ Gene Expression Assay (FAM)	*Cdkn1a*	Mm04205640_g1	4331182
TaqMan™ Gene Expression Assay (FAM)	*Cdkn2a*	Mm00494449_m1	4331182
TaqMan™ Gene Expression Assay (FAM)	*Lmnb1*	Mm00521949_m1	4331182

Supplementary Alms1 Mouse Model Information

Table S4. Comparison of Current and Previous *Alms1* knockout mouse models.

Abbreviations: bp, basepairs; ENU, N-ethyl-N-nitrosourea; ES cell, embryonic stem cell; GKO, global knockout; HFD, high-fat diet; MSC KO, MSC-specifical Alms1 knockout; p15.5, postnatal day 15.5; WT, wild-type.

Mouse model	**Alms1$^{GT/GT}$**	**Alms1$^{foz/foz}$ (fat aussie)**	**Alms1^{L2131X}**	**Alms1$^{flin/flin}$** and **Alms$^{flin/flin}$; Adipo-Cre$^{+/-}$**	**Alms1 GKO** and **Alms1 MSC KO**
Generation method	Gene trap in intron 13 [1]	Spontaneous 11 bp deletion in exon 8 [2]	ENU-induced; nonsense mutation in exon 10 [3]	Alms1$^{(EUCOMM)tm1e}$ [4]	Alms1$^{(EUCOMM)tm1c}$ and Alms1$^{(EUCOMM)tm1d}$ [5]
Alms1 KO validation method	qPCR for *Alms1* and SDS-PAGE of PCR amplicons [1]	cDNA sequencing and SDS-PAGE of PCR amplicons [2]	cDNA sequencing [3]	qPCR for *Alms1* and SDS-PAGE of PCR amplicons [4]	qPCR for *Alms1* and SDS-PAGE of PCR amplicons [5]
Mouse back-ground	Gene trap in 129 ES cell. Mice then backcrossed onto C57BL/6J for 1 generation [1], and later for 10 more generations [6]. Also crossed onto C57BL6/Ei background [7].	NOD/B10 background [8]. Also backcrossed onto BALB/c and C57BL6/J [9].	Mixed C57Bl6/NOD genetic background [3]	C57Bl6/N [4]	C57Bl6/N [5]
First published	2005 [1]	2006 [8]	2007 [3]	2020 [4]	This publication
Sexes studied	Both	Both	Both	Males only [4]	Both [5]
Heterozygous phenotype	Same as WT [1]	Same as WT [8]	Same as WT [3]	Not reported	Not studied
Diet	Chow [1], [7]	Chow and HFD [8]	Not reported [3]	Chow [4]	45% fat diet [5]
Appetite	Not reported	Hyperphagia from 60 days of age [8]	Not reported	Not reported	Hyperphagia [5]

Body weight	Obese. Divergence in body weight from WT at 8-12 weeks of age [1], [7]	Body mass increased [8]; Obese, divergence around 12 weeks of age [10]	Greater body weight than WT. Divergence from WT at 7-10 weeks of age [3]	Greater body weight at 3 months of age in Alms1$^{flin/flin}$ [4]	Greater body weight than WT from 10-12 weeks [5]
Fat mass	Fat pads heavier than WT [1], [7]. Enlarged adipocyte size/hypertrophy [7].	Higher percentage fat mass and heavier adipose depots [10], [11].	Greater than WT. Hypertrophy of adipose tissue seen [3].	Not reported	Higher body fat mass from 10 weeks and heavier fat pads at 24 weeks [5]
Lean mass	Not reported	Increased lean mass at 250 days of age [8]	Same as WT [3]	Not reported	Same as WT [5]
Fasting blood glucose	Males hyperglycaemic from 16 weeks [1]	Hyperglycaemia in older mice [8]	Same as WT [3]	Alms1$^{flin/flin}$ hyperglycaemic at 3 months [4]	Mild hyperglycaemia [5]
Serum insulin	Hyperinsulinemia [1], [7]	Hyperinsulinaemia (preceeding hyperglycaemia) [8], [10]	Hyperinsulinaemia [3]	Not reported	Hyperinsulinaemia [5]
Serum triglyceride	Same as WT [1], [7]	Same as WT [8], [10]	Elevated [3]	Not reported	Same as WT [5]
Serum cholesterol	Elevated [1], [7]	Elevated [8], [10]	Elevated [3]	Not reported	Elevated [5]
Brown fat	Not reported	Heavier BAT with higher fat content, lower mitochondrial density [12]	Higher lipid content in iBAT [3]	Not reported	Heavier BAT due to increased lipid content in females but not males [5]
Liver	Hepato-megaly and steatosis [4]	Enlarged and steatotic [11]; steatohepatitis on HFD [16]	Steatosis [6]	Not reported	Hepatomegaly and steatosis in both GKO and MSC KO [8]
Kidney	Enlarged & heavier; dilated proximal tubules [4]	Not reported	Dilated tubules in cortex [6]	Not reported	Enlarged & heavier (data not published)
Pancreas	Not reported	Islet hyperplasia [11]	Not reported	Not reported	Not investigated
Vision	Impaired [4]	Impaired; degeneration with age [17]	Defective rhodopsin transport in	Not reported	Not investigated

			retina [6]		
Hearing	Impaired [4], [9]	Impaired [11]	Not reported	Not reported	Not investigated
Fertility	Hypogonadism in males: atrophic seminiferous tubules, no sperm heads [4]	Males infertile; testes smaller; decreased germ cells; dysfunctional sperm [11]	Reduced germinal cells in testis; reduced numbers and shorter sperm flagella [6]	Not reported	Not investigated
Heart	P15.5 hearts greater size, larger cardiomyocytes and markers of proliferation detected [18]	Not reported	Not reported	Not reported	No change detected at p15.5. Evidence of restrictive cardiomyopathy at 23 weeks of age in females but not males.

Supplementary References

[1] J. Grune *et al.*, "Accurate assessment of LV function using the first automated 2D-border detection algorithm for small animals - evaluation and application to models of LV dysfunction," *Cardiovascular Ultrasound*, vol. 17, no. 1, p. 7, 2019, doi: 10.1186/s12947-019-0156-0.

[2] A. E. Hein and U. Bodendorf, "Real-time PCR: duplexing without optimization.," *Anal Biochem*, vol. 360, no. 1, pp. 41–46, Jan. 2007, doi: 10.1016/j.ab.2006.10.016.

[3] M. W. Pfaffl, "A new mathematical model for relative quantification in real-time RT-PCR.," *Nucleic Acids Res*, vol. 29, no. 9, p. e45, May 2001, doi: 10.1093/nar/29.9.e45.

[4] G. B. Collin *et al.*, "Alms1-disrupted mice recapitulate human Alström syndrome," *Hum Mol Genet*, vol. 14, no. 16, pp. 2323–2333, Aug. 2005, doi: 10.1093/hmg/ddi235.

[5] T. Arsov *et al.*, "Fat aussie--a new Alstrom syndrome mouse showing a critical role for ALMS1 in obesity, diabetes, and spermatogenesis," *Mol Endocrinol*, vol. 20, no. 7, pp. 1610–1622, 2006, doi: 10.1210/me.2005-0494.

[6] G. Li *et al.*, "A role for Alström syndrome protein, Alms1, in kidney ciliogenesis and cellular quiescence," *PLoS Genet*, vol. 3, no. 1, p. e8, Jan. 2007, doi: 10.1371/journal.pgen.0030008.

[7] T. Geberhiwot *et al.*, "Relative Adipose Tissue Failure in Alström Syndrome Drives Obesity-Induced Insulin Resistance," *Diabetes*, vol. 70, no. 2, pp. 364–376, Feb. 2021, doi: 10.2337/db20-0647.

[8] E. J. McKay *et al.*, "Mesenchymal-specific Alms1 knockout in mice recapitulates key metabolic features of Alström Syndrome," *bioRxiv*, p. 2023.10.12.562074, Jan. 2023, doi: 10.1101/2023.10.12.562074.

[9] D. Jagger *et al.*, "Alström Syndrome protein ALMS1 localizes to basal bodies of cochlear hair cells and regulates cilium-dependent planar cell polarity," *Hum Mol Genet*, vol. 20, no. 3, pp. 466–481, Feb. 2011, doi: 10.1093/hmg/ddq493.

[10] F. Favaretto *et al.*, "GLUT4 defects in adipose tissue are early signs of metabolic alterations in alms1GT/GT, a mouse model for obesity and insulin resistance," *PLoS One*, vol. 9, no. 10, p. e109540, Oct. 2014, doi: 10.1371/journal.pone.0109540.

[11] T. Arsov *et al.*, "Fat aussie - A new Alström syndrome mouse showing a critical role for ALMS1 in obesity, diabetes, and spermatogenesis," *Molecular Endocrinology*, vol. 20, no. 7, pp. 1610–1622, 2006, doi: 10.1210/me.2005-0494.

[12] G. C. Farrell *et al.*, "Strain dependence of diet-induced NASH and liver fibrosis in obese mice is linked to diabetes and inflammatory phenotype," *Liver International*, vol. 34, no. 7, pp. 1084–1093, Aug. 2014, doi: 10.1111/liv.12335.

[13] C. Z. Larter *et al.*, "Roles of adipose restriction and metabolic factors in progression of steatosis to steatohepatitis in obese, diabetic mice," *J Gastroenterol Hepatol*, vol. 24, no. 10, pp. 1658–1668, Oct. 2009, doi: 10.1111/j.1440-1746.2009.05996.x.

[14] C. Z. Larter, M. M. Yeh, D. M. van Rooyen, J. Brooling, K. Ghatora, and G. C. Farrell, "Peroxisome proliferator-activated receptor-α agonist, Wy 14643, improves metabolic indices, steatosis and ballooning in diabetic mice with non-alcoholic steatohepatitis," *Journal of Gastroenterology and Hepatology (Australia)*, vol. 27, no. 2, pp. 341–350, Feb. 2012, doi: 10.1111/j.1440-1746.2011.06939.x.

[15] L. Poekes *et al.*, "Defective adaptive thermogenesis contributes to metabolic syndrome and liver steatosis in obese mice," *Clin Sci*, vol. 131, no. 4, pp. 285–296, Feb. 2017, doi: 10.1042/CS20160469.

[16] T. Arsov *et al.*, "Adaptive failure to high-fat diet characterizes steatohepatitis in Alms1 mutant mice," *Biochem Biophys Res Commun*, vol. 342, no. 4, pp. 1152–1159, Apr. 2006, doi: 10.1016/j.bbrc.2006.02.032.

[17] A. Brun *et al.*, "In vivo phenotypic and molecular characterization of retinal degeneration in mouse models of three ciliopathies," *Exp Eye Res*, vol. 186, Sep. 2019, doi: 10.1016/j.exer.2019.107721.

[18] L. T. Shenje *et al.*, "Mutations in Alström protein impair terminal differentiation of cardiomyocytes," *Nat Commun*, vol. 5, no. 1, p. 3416, May 2014, doi: 10.1038/ncomms4416.